Vibrational excitation in the $e + CO_2$ system: Analysis of the two-dimensional energy-loss spectrum

Jan Dvořák,[1,*] Miloš Ranković,[2] Karel Houfek,[1] Pamir Nag,[2] Roman Čurík,[2] Juraj Fedor,[2] and Martin Čížek[1,†]

[1]*Charles University, Faculty of Mathematics and Physics, Institute of Theoretical Physics, V Holešovičkách 2, 180 00 Prague 8, Czech Republic*

[2]*J. Heyrovský Institute of Physical Chemistry, Czech Academy of Sciences, Dolejškova 2155/3, 182 23 Prague 8, Czech Republic*

(Received 8 October 2022; accepted 16 November 2022; published 7 December 2022)

We present a detailed analysis of the two-dimensional electron energy-loss spectrum of CO_2, which extends our recent Letter [Phys. Rev. Lett. **129**, 013401 (2022)]. We show that our vibronic coupling model [Phys. Rev. A **105**, 062821 (2022)] captures primary features of the multidimensional dynamics of the temporary molecular anion, and the calculations qualitatively reproduce the spectrum. The shape of the spectrum is given by two overlapping contributions that originate in excitation of vibrational states within Σ_g^+ and Π_u Fermi polyads. Propensity rules in terms of scattered and vibrational wave functions are also discussed to clarify the selectivity of states from the vibrational pseudocontinuum that is responsible for the observed fine structure.

DOI: 10.1103/PhysRevA.106.062807

I. INTRODUCTION

The low-energy (<5 eV) inelastic electron scattering from the CO_2 molecule

$$e + CO_2 \rightarrow CO_2^- \rightarrow e + CO_2^* \tag{1}$$

is full of interesting phenomena. The experimental effort to probe this system goes back as far as the 1920s by Ramsauer [1]. In the 1960s and 1970s, Boness and Schulz [2–4] and Čadež *et al.* [5,6] thoroughly studied the 3–5 eV region dominated by a $^2\Pi_u$ resonance. Observed peaks in the energy-loss spectra were attributed to the $(n, 0^0, 0)$ and $(n, 1^1, 0)$ vibrational progressions. The energy dependence of the vibrational cross sections revealed an oscillatory structure, which they correctly recognized as the boomerang oscillations and even reproduced [6] by one-dimensional (1D) calculations for the symmetric stretching using the local complex potential (LCP) model developed by Herzenberg [7]. They also studied the shift of the boomerang peaks towards higher incident energies with energy loss, which explains the diagonal rays later observed in the two-dimensional (2D) energy-loss spectrum, see below. The LCP nuclear dynamics was further studied by Kazansky and Sergeeva [8,9], who also included the bending motion.

By improving the signal-to-noise ratio, Allan [10] divided the energy-loss spectra into three regions. Region I was dominated by the $(n, 0^0, 0)$ progression (for a small scattering angle). Region II showed a complex structure. Well distinguishable broad peaks reappeared at high energy losses (region III) with positions that did not correspond to the $(n, 0^0, 0)$ progression. Using the 2D scanning technique developed by Reddish *et al.* [11], Currell and Comer [12–14] recorded the first 2D energy-loss spectrum of CO_2. They fully realized the importance of the Fermi resonance effect on neutral vibrational states [15,16] and argued that the excitation of fairly linear states and highly bent states within Σ_g^+ polyads was responsible for the two newly observed structures (labeled by *A* and *B*).

Itikawa *et al.* [17] and Kochem *et al.* [18] probed the increase of the cross sections near the threshold, see also references therein for earlier works. They showed that the direct dipole scattering explains well the threshold peaks of the $(0, 1^1, 0)$ bending and $(0, 0^0, 1)$ asymmetric stretching modes whereas the *s*-wave scattering effected by a $^2\Sigma_g^+$ virtual state is largely responsible for the $(1, 0^0, 0)$ symmetric stretching excitation. The effect of the virtual state was studied by many theoretical methods, such as coupled-channel calculations of Morrison *et al.* [19,20], two-state model by Whitten and Lane [21], discrete-state-in-continuum model by Estrada and Domcke [22] or the energy-modified adiabatic phase matrix method by Mazevet *et al.* [23].

From a plethora of *ab initio* fixed-nuclei calculations, we emphasize the work of Morgan [24], who located the *S*-matrix poles in the complex plane corresponding to the $^2\Sigma_g^+$ virtual state and both Renner-Teller components of the $^2\Pi_u$ shape resonance. Other works include Morrison *et al.* [19], Lee *et al.* [25], and Rescigno *et al.* [26]. The angular dependence of the differential cross sections was also studied by many groups: Register *et al.* [27], Kochem *et al.* [18], Antoni *et al.* [28], Cartwright *et al.* [29], and Kitajima *et al.* [30,31].

Thanks to the improvement of the energy resolution down to 7 meV, Allan [32,33] revealed a strong selectivity in excitation of individual members of the Fermi polyads. Such a behavior in the $^2\Pi_u$ region was reproduced by McCurdy *et al.* [34,35], who performed time-dependent 2D LCP calculations [36] with both Renner-Teller states. Shortly after, Vanroose *et al.* [37] explained the selectivity at the threshold using a 2D effective-range potential model [38,39]. Recently, Laporta *et al.* [40] reported 1D LCP calculations considering each vibrational mode independently.

*jan.dvorak@utf.mff.cuni.cz
†martin.cizek@mff.cuni.cz

Despite the theoretical effort that the $e + CO_2$ system have received, the shape of the spectrum for moderate and high energy losses is still not explained. Furthermore, we are not aware of any dynamical calculations of this system that predict the excitation of nontotally symmetric vibrational states such as states with odd quanta of bending or asymmetric stretching. Such states can be excited due to the vibronic coupling in the resonant electron-molecule scattering, as was investigated by Gallup [41]. He showed that the first-order terms in the electron-molecule potential give the selection rules formulated by Wong and Schulz [42] to explain the spectrum of benzene. The symmetries of expected excited vibrational states are those that belong (i) to the symmetrized square of the irreducible representation of the resonance, or (ii) to the irreducible representation of the resonance, which leads to the outgoing s-wave electron.

The two-state discrete momentum representation method developed by Čurík and Čársky [43] have been used to study the inelastic electron scattering from polyatomic molecules, such as methane [44], diacetylene [45], and cyclopropane [46]. In the case of cyclopropane, Čurík *et al.* [46] showed that excitation of the ν_4 twist mode does not follow the selection rules because the incoming f wave is transformed to a p wave. Gallup [41] concluded that higher orders cause excitation of additional symmetries but the relations become too complicated to be useful.

The present paper concludes our study of vibrational excitation of the CO_2 molecule by slow electrons. Our joint experimental and theoretical work is summarized in a recent letter [47], which will be referred to as the Letter throughout this paper. The detailed description of our work is then divided in two parts. Reference [48] (referred to as Paper I in the following text) discusses the derivation of the theoretical model dictated by the symmetry of the system, together with the determination of the model parameters by fitting the results of our fixed-nuclei electron-molecule scattering calculations for a large set of geometries. Paper I also describes the computational procedure based on Krylov subspace iteration methods to find the wave function of the anion and the formulas for calculation of the vibrational excitation cross sections. Here, we focus on a detailed presentation of the results of our calculations including the comparison with our and previous experimental data.

The paper is organized as follows: Section II describes the experimental setup used to measure the energy-loss spectra, which are also shown there. Section III discusses the grouping of neutral vibrational states into polyads. In Sec. IV, we summarize and emphasize the key theoretical points that are important for the subsequent discussion. The calculated spectra are presented in a similar way as the experimental data in Sec. V. Then, we analyze the energy-loss spectra based on various aspects (symmetry of final states, electron partial waves, angular dependence, etc.) and examine the underlying mechanisms in terms of wave functions in Sec. VI, where the cross sections for low-lying states are also shown. In Sec. VII, we study the sensitivity of the calculations to parameters of the model and finally our work is concluded in Sec. VIII by summarizing the results and discussing possible improvements and applications of the approach to another systems.

II. EXPERIMENTAL SPECTRA

The electron energy-loss spectra were recorded on the electrostatic spectrometer [49,50]. The electrons were emitted from a heated iridium filament and energy-selected by a double-hemispherical electron monochromator. The incident electron energy ϵ_i was controlled by floating the monochromator with respect to the potential of the collision region. The electrons were scattered on the effusive beam of the CO_2 gas and their residual energy ϵ_f was analyzed with a double-hemispherical electron analyzer. The analyzer can be rotated in order to probe various scattering angles. The energy of the incident beam was calibrated on the 2^2S resonance in helium at 19.365 eV. Electron-energy resolution was 18 meV, as determined from the width of the elastic peak.

All the spectra presented here were recorded in a *constant-ϵ_i* mode where the incident energy was fixed, the residual energy was scanned, and the signal was plotted as a function of the energy loss $\Delta\epsilon = \epsilon_i - \epsilon_f$. Figure 1 shows a two-dimensional (2D) energy-loss spectrum recorded at the 135° scattering angle. It is constructed from individual 1D energy-loss spectra recorded at 220 incident electron energies with 10 meV increments. Such color-coded map can reveal complex dynamics of nuclear motion induced by the electron scattering [51–54]. The individual features of our 2D spectrum for CO_2 are outlined in the Letter and further discussed in the following sections.

To better understand the detailed structure of the spectrum, Fig. 2 shows the individual electron energy-loss spectra at four selected incident energies (horizontal sections of 2D spectrum) but separately recorded for a better signal-to-noise ratio. The spectra in both figures were recorded at high scattering angle to enhance the resonance processes with respect to direct-dipole excitations. It is well known that direct excitation processes related to direct-dipole excitation have cross sections peaking at small scattering angles [10,55], the resonant processes are thus most pronounced in the backscattering direction. The 135° angle is the highest mechanical angle achievable with the present setup.

Before proceeding to the calculated spectra, we discuss the vibrational states of the neutral CO_2 molecule and their energies since they are directly related to the energy-loss axis of the spectra.

III. VIBRATIONAL STATES OF NEUTRAL CO_2

The vibrational states of the CO_2 molecule within the harmonic approximation are identified by four numbers [16]:

$$\nu \equiv \left(\nu_g, \nu_b^{\ell_b}, \nu_u\right), \tag{2}$$

where ν_g, ν_b, and ν_u denote numbers of quanta in symmetric stretching, bending, and asymmetric stretching, respectively, and ℓ_b is the angular momentum of the bending motion with respect to the molecular axis. The corresponding experimental vibrational frequencies are $\omega_g = 167.5$ meV, $\omega_u = 297.1$ meV, and $\omega_b = 83.3$ meV [56].

Although the anharmonic corrections are important for the understanding of the spectrum of the neutral CO_2, we start with the harmonic basis because it is used in our numerical

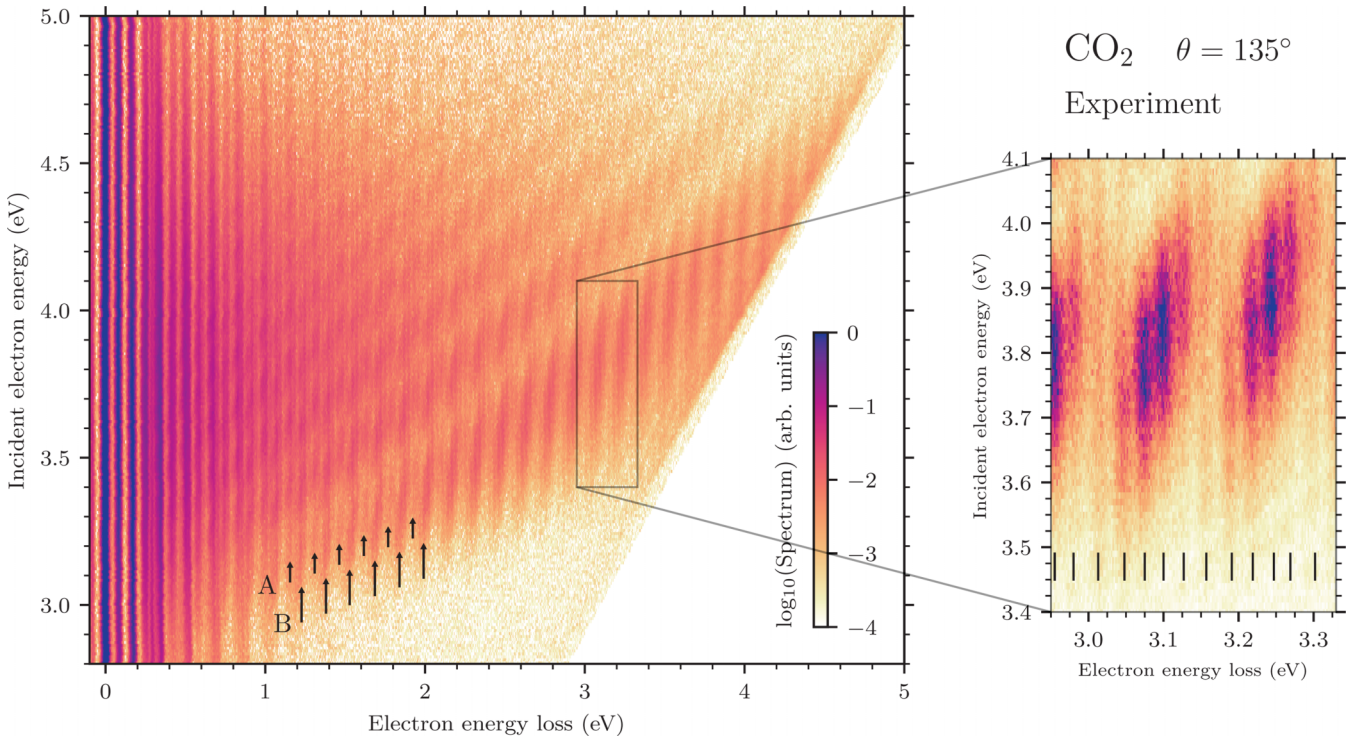

FIG. 1. Experimental 2D electron energy-loss spectrum of CO_2 for a scattering angle of 135°. A detail of the spectrum is shown in a linear scale from 0 to 1 and the fine structure is indicated (average spacing ∼29 meV). Structures *A* and *B* observed by Currell and Comer [12–14] are labeled in the main plot.

treatment of the dynamics as discussed in Paper I and here below.

For the later discussion it is important to remind the classification of the states according to the irreducible representations of the molecular symmetry group $D_{\infty h}$ [16]. The angular momentum is determined by ℓ_b and the parity is given by the product $\nu_u \nu_b$. Thus, the states $|\nu\rangle$ correspond to the Σ_g^+ and Σ_u^+ representations for $\ell_b = 0$ with ν_u even and ν_u odd, respectively, to Π_u or Π_g for $\ell_b = 1$ with ν_u even or odd, to Δ_g or Δ_u for $\ell_b = 2$ with ν_u even or odd, and so on.

A. Harmonic polyads

The energies of one quantum of symmetric stretching and two bending quanta are almost degenerate ($\omega_g - 2\omega_b = 0.9$ meV). Therefore, the harmonic states are naturally organized into groups (polyads) with nearly the same energy. The harmonic energy of the state $|\nu\rangle$ reads

$$E_\nu = E_0 + \nu_g \omega_g + \nu_b \omega_b + \nu_u \omega_u, \tag{3}$$

where E_0 is the ground-state energy, ν_g and ν_u attain values $0, 1, 2, \ldots$ and $\nu_b = \ell_b, \ell_b + 2, \ell_b + 4, \ldots$. As a result, all harmonic states $|\nu\rangle$ for

$$\nu = \left(\nu_g, \nu_b^{\ell_b}, \nu_u\right) = [n, (2m + \ell_b)^{\ell_b}, \nu_u], \tag{4}$$

where $n + m = N = \text{const.}$, have the energy close to the value

$$E_\nu \simeq E_0 + N\omega_g + \ell_b \omega_b + \nu_u \omega_u, \tag{5}$$

with a spread of $0.9N$ meV. For example, the Σ_g^+ dyad ($N = 1$) with $\nu_u = 0$ contains two harmonic states $(1, 0^0, 0)$ and $(0, 2^0, 0)$ while the harmonic Π_u polyad with $N = 10$ consists of eleven states $(10, 1^1, 0)$, $(9, 3^1, 0)$, ..., $(0, 21^1, 0)$.

Considering the energy-loss range of the experimental data (Fig. 1), the maximum N that we need to take into account is $N = 30$. The energy spread of the states within individual harmonic polyads is thus less then $0.9N \simeq 30$ meV. The 2D spectrum in Fig. 1 below energy loss $\Delta\epsilon < 1$ eV is clearly organized into polyads but the quasicontinuous character of the spectrum at higher electron energy losses is inconsistent with this estimate for the energy spread.

B. Fermi-coupled states

The inconsistency is not surprising since it is well known that the vibrational states of neutral CO_2 are significantly influenced by the Fermi resonance effect [15,16]. Anharmonic corrections to the potential-energy surface split the nearly degenerate harmonic states of the same symmetry and also correlate the vibrational motion in the symmetric stretching and bending directions mixing the different states within the polyads.

To calculate these proper final vibrational states, we employ the Hamiltonian of Chedin [57], which includes the anharmonic corrections. The Fermi-coupled states $|\nu_{\rm FR}\rangle$, for the symmetry given by fixed values of ℓ_b and ν_u, are expanded into linear combinations of harmonic states:

$$|\nu_{\rm FR}\rangle = \sum_\nu c_\nu |\nu\rangle, \tag{6}$$

where the coefficients c_ν are obtained by diagonalizing the anharmonic vibrational Hamiltonian [57]. In principle, the

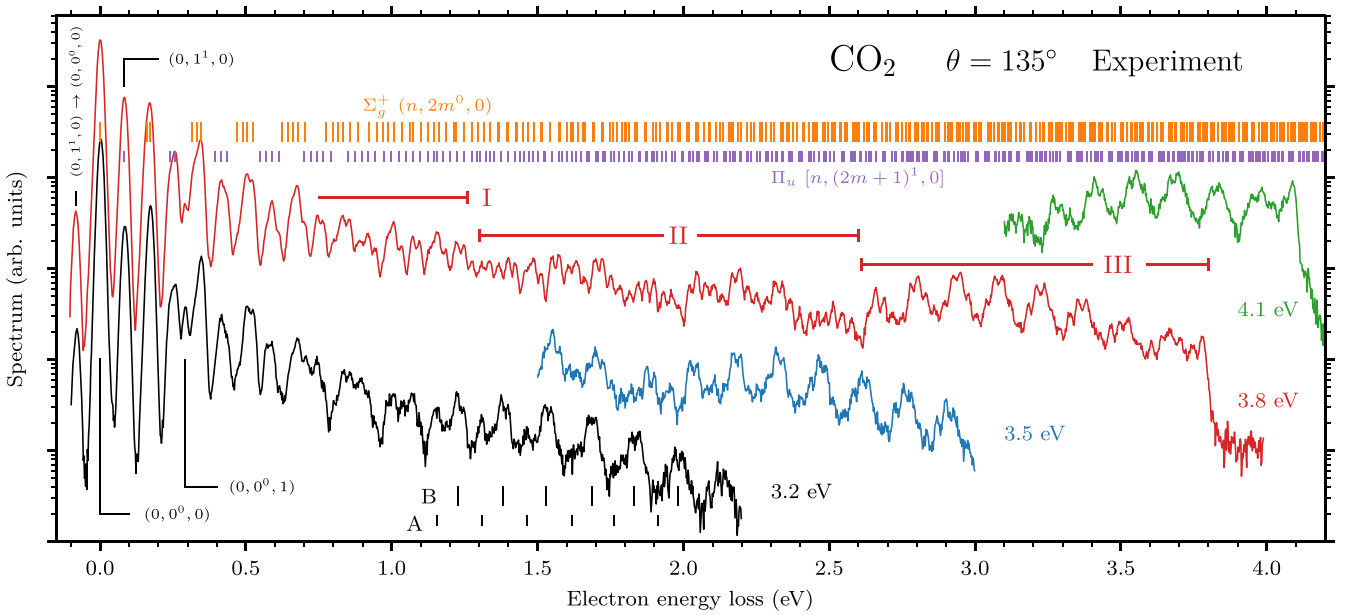

FIG. 2. Experimental 1D energy-loss spectra for a scattering angle of 135° and incident electron energies 3.2, 3.5, 3.8, and 4.1 eV. The spectra are shown on the logarithmic scale but lines for different incident energies are arbitrarily shifted with respect to each other. Calculated energies of Fermi-coupled vibrational states that belong to Σ_g^+ $(n, 2m^0, 0)$ and Π_u $[n, (2m+1)^1, 0]$ polyads $(n+m = 0, 1, \ldots)$ are shown. Regions of order, chaos, and order observed by Allan [10] are labeled by I, II, and III for the 3.8 eV spectrum. Positions of *A* and *B* structures observed by Currell and Comer [12–14] are indicated for the 3.2 eV spectrum.

sum runs over all allowed ν_g, ν_b but the results show that the coupling among polyads with different values of N is negligible for the range of vibrational energies considered in this study. We can thus identify the Fermi-coupled states by specifying numbers ℓ_b, ν_u, and N to determine the specific polyad $[n, (2m+\ell_b)^{\ell_b}, \nu_u]$ of harmonic states. After the diagonalization, the Fermi-coupled states are sorted by their energy. The individual state can be referred to by a symbol $N(i)$, which denotes the ith state in the polyad $N = n + m$. Note that the ground state $\nu_i = (0, 0^0, 0)$, i.e., the initial vibrational state ν_i, is subject to no anharmonic corrections and thus belongs to both the harmonic- and the Fermi-coupled sets of states.

The anharmonic energies ϵ_{FR} emerging from the Σ_g^+ $(n, 2m^0, 0)$ and Π_u $[n, (2m+1)^1, 0]$ polyads are shown in Fig. 2 by a grid of small vertical lines displayed in the upper part of the figure. The positions of the low energy-loss peaks correspond approximately to the middle of the polyads, but above $\Delta\epsilon \approx 0.9$ eV the energy ranges of the individual polyads start to overlap. At high energy losses, the spectrum of the Fermi-coupled states is dense and rather erratic and so there is no obvious connection between individual experimental peaks and the vibrational energies. We conclude that either polyads with nonzero ν_u have to be involved or there is some selective mechanism that allows excitation of only certain states from the pseudocontinuum.

To gain more insight into the Fermi coupling and the correlation of the bending and stretching motion within the polyads, we plot the wave functions of selected states in Fig. 3. The first column shows the shape of the lowest $(i = 1)$ and highest $(i = 14)$ states together with some states from the middle $(i = 5, 6, 11)$ for the Σ_g^+ polyad with $N = 13$, and similarly, other two columns contain the wave functions from Π_u polyads with $N = 13$ and 19. The wave functions are plotted with respect to the normal coordinates used in the dynamics, see Sec. IV and Note 1.

Small bending correlates to positive symmetric stretching (prolongation of the C-O bonds) for the lowest states within each polyad (first row in Fig. 3) while the highest states are more spread in the bending direction (highly bent states) with negative stretching values at small bending. The middle states have rather intriguing shapes but overall the probability density is localized in the vicinity of the stretching axis (linear states). Note that the harmonic states would have nodal planes parallel with the coordinate axes since there is no correlation between stretching and bending, in contrast to the behavior seen here for the coupled states.

To somehow quantify the shape of the wave functions, we characterize each Fermi-coupled state by a simple quantity, the mean value of the number of symmetric stretching quanta

$$\langle \nu_g \rangle = \sum_{\nu} \nu_g |c_\nu|^2, \tag{7}$$

where the sum runs over all harmonic states within the particular polyad, c_ν are the expansion coefficients in the harmonic basis [Eq. (6)], and ν_g is the symmetric stretching coordinate of the ν vector [Eq. (2)]. The mean value $\langle \nu_g \rangle$ therefore describes the amount of symmetric stretching.

Similarly, we can define the mean value for bending quanta

$$\langle \nu_b \rangle = \sum_{\nu} \nu_b |c_\nu|^2, \tag{8}$$

but the two values are not independent due to the relation $n + m = N$. Larger values of $\langle \nu_b \rangle$ thus corresponds to smaller $\langle \nu_g \rangle$ and vice versa. The quantity $\langle \nu_g \rangle$ is also shown in Fig. 3

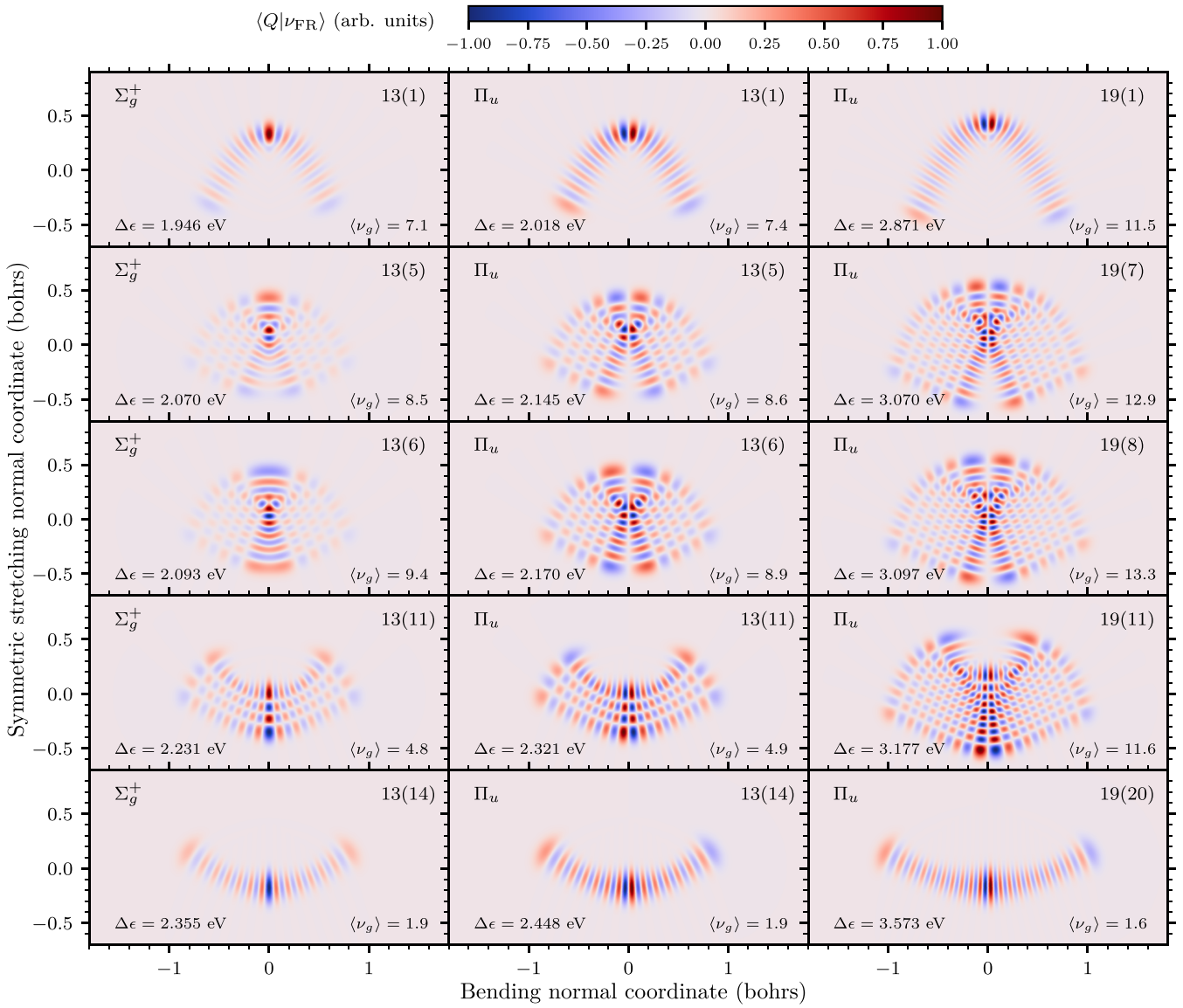

FIG. 3. Fermi-coupled vibrational wave functions upon symmetric stretching and bending (asymmetric stretching coordinate is set to zero). The first two columns show states $N(i)$ for $i = 1, 5, 6, 11, 14$ (from top), belonging to the Σ_g^+ $(n, 2m^0, 0)$ and Π_u $[n, (2m+1)^1, 0]$ Fermi polyads with $N = n + m = 13$, respectively. The third column shows states $N(i)$ for $i = 1, 7, 8, 11, 20$ (from top), within the Π_u polyad with $N = n + m = 19$. The energy loss $\Delta\epsilon$ and the mean value of number of symmetric stretching quanta $\langle\nu_g\rangle$ are also shown for each state. The wave functions are independently normalized.

together with the energy loss $\Delta\epsilon_{FR}$ for each state (when excited by an electron from the ground vibrational state).

IV. THEORY

Our theoretical model is discussed in detail in Paper I. For convenience, we summarize the basic aspects of the theory used in the discussion of the results in this paper.

A. Nonlocal model of vibronic dynamics

The model is designed to treat the vibronic dynamics of vibrational excitation of the CO_2 molecule in its ground electronic $^1\Sigma_g^+$ state by low-energy electrons, see Eq. (1). The process is mediated by three states of the temporary molecular anion CO_2^-: the $^2\Sigma_g^+$ virtual state and the double-degenerate $^2\Pi_u$ shape resonance.

These anionic states are assumed to be diabatic with respect to the vibrational motion described by normal coordinates Q_g, Q_u, and $Q_\pm = Q_x \pm iQ_y$. We refer to these states as discrete electronic states $|d\rangle$, $d \in \{\Pi_+, \Sigma, \Pi_-\}$.

The vibronic dynamics of the CO_2^- is described by a three-component wave function

$$|\Psi\rangle = \begin{pmatrix} |\psi_{\Pi_+}\rangle \\ |\psi_\Sigma\rangle \\ |\psi_{\Pi_-}\rangle \end{pmatrix} = \sum_d |\psi_d\rangle|d\rangle, \tag{9}$$

where the components $|\psi_d\rangle$ are functions of the vibrational coordinates expanded in the basis of neutral harmonic

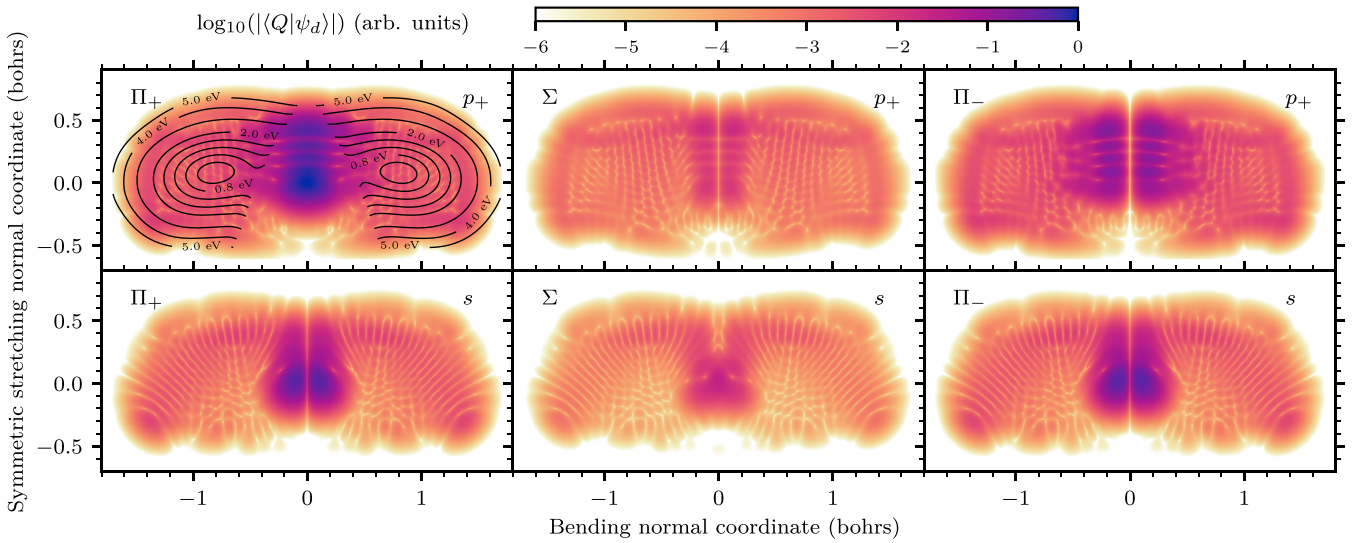

FIG. 4. Vibrational components $\langle Q|\psi_d\rangle$ of the scattering wave function $|\Psi\rangle$ that belongs to the discrete states $|d\rangle$, $d = \Pi_+, \Sigma$, and Π_- upon symmetric stretching and bending (asymmetric stretching coordinate is set to zero). The shown wave function $|\Psi\rangle$ is the solution of Eq. (10) for incident electron energy of 3.8 eV and for incoming electron partial waves p_+ (first row) and s (second row). The components are all normalized with respect to the global maximum. The contours in the top-left panel represent the lowest adiabatic potential-energy surface of CO_2^- for geometries where it is bound and the energies are given with respect to the minimum of the neutral potential.

vibrational states defined in Appendix A of Paper I. The wave function $|\Psi\rangle$ is found by solving the inhomogeneous Schrödinger equation

$$[(E - H_0)\mathbb{1} - U - F(E - H_0)]|\Psi\rangle = |\Phi\rangle, \qquad (10)$$

where E is the total energy conserved during the collision, H_0 is the vibrational Hamiltonian of the neutral molecule in the harmonic approximation, $U = \{U_{dd'}\}$ is the 3×3 matrix describing the diabatic potential-energy surfaces and the direct vibronic coupling of the discrete states, and $F(E - H_0)$ is the nonlocal operator matrix giving the indirect vibronic coupling through the electron continuum.

The right-hand side of the Schrödinger equation,

$$|\Phi\rangle = \begin{pmatrix} V^{\mu_i}_{\Pi_+\epsilon_i}|\nu_i\rangle \\ V^{\mu_i}_{\Sigma\epsilon_i}|\nu_i\rangle \\ V^{\mu_i}_{\Pi_-\epsilon_i}|\nu_i\rangle \end{pmatrix}, \qquad (11)$$

describes the vertical attachment of the incoming electron with energy ϵ_i to CO_2 in its ground vibrational state $|\nu_i\rangle$, where the energy-dependent amplitudes $V^{\mu_i}_{d\epsilon}$ control the coupling between the discrete states $|d\rangle$ and the partial-wave components $\mu_i \equiv (l, m)$ of the incoming electron.

To obtain the energy-loss spectra discussed below we solved the Schrödinger equation Eq. (10) for 1500 incident energies $\epsilon_i \in [0.001, 5.0]$ eV and for each included incoming electron partial wave μ_i. An example of these wave functions for $\epsilon_i = 3.8$ eV and $\mu_i = s$ and p_+ is shown in Fig. 4, where the absolute value of $|\psi_d\rangle$ is plotted as a function of symmetric stretching and bending coordinates.[1]

The electron autodetachment from CO_2^- into neutral CO_2 in the vibrational state $|\nu_f\rangle$ is controlled by the amplitude (an element of the T matrix)

$$T_{\nu_f\mu_f\leftarrow\nu_i\mu_i} = \sum_d \langle\nu_f|V^{\mu_f *}_{d\epsilon_f}|\psi_d\rangle. \qquad (12)$$

We calculated the T matrix for all 1500 values of the incident energy ϵ_i, all partial waves and all accessible harmonic final states $|\nu_f\rangle$ (about 8000 states). These values are stored and both integral and differential cross sections for all final states and angles, as well as 2D electron energy-loss spectra for any scattering angle can be obtained from these matrices in a fast postprocessing procedure, see below.

B. Symmetry considerations for the dynamics and final states

Before proceeding to the actual discussion of the calculated spectra, we would like to comment on the symmetry in the process of vibrational excitation of CO_2, which is closely related to conservation of angular momentum and parity. These principles have already been discussed in Paper I since they are important in the construction of the model, but we need to add a few remarks that are important for the following discussion of the results.

[1]The two-dimensional bending can be described by the Cartesian normal coordinates Q_x and Q_y, their complex combinations $Q_\pm = Q_x \pm iQ_y$, or by polar coordinates (ρ, φ) where ρ represents the magnitude of the bending and φ the orientation of the molecular plane, see Sec. II B 1 in Paper I. We plot the wave functions (anionic or vibrational shown above) with respect to the magnitude of the bending measured in bohrs and we set $\varphi = 0$. The dependence on φ gives only an overall phase factor $\exp(i\ell_b\varphi)$ because ℓ_b is fixed for any given vibrational state of CO_2 or one vibrational component $|\psi_d\rangle$ of the anionic wave function.

TABLE I. Correlation of the symmetry of the electronic and vibrational parts of the wave function resulting from the conservation of angular momentum and parity. Rows correspond to partial waves of the incident electron. The first block (columns 2–4) gives the symmetry of the vibrational parts $|\psi_d\rangle$ for the three discrete states $|d\rangle$. The second block shows the vibrational symmetry of the resulting CO_2 when the electron leaves as partial wave μ_f.

	$\|\psi_d\rangle$ for d			$\|\nu_f\rangle$ for μ_f			
μ_i	Π_+	Σ	Π_-	s	p_z	p_+	p_-
s	Π_u	Σ_g^+	Π_u	Σ_g^+	Σ_u	Π_u	Π_u
p_z	Π_g	Σ_u^+	Π_g	Σ_u^+	Σ_g^+	Π_g	Π_g
p_+	Σ_g^+	Π_u	Δ_g	Π_u	Π_g	Σ_g^+	Δ_g
p_-	Δ_g	Π_u	Σ_g^+	Π_u	Π_g	Δ_g	Σ_g^+

The total electron and nuclear symmetry of the $e + CO_2$ system is conserved during the collision. Since the neutral molecule is initially in the ground electronic and ground vibrational states, which are both totally symmetric, the total symmetry is exclusively given by the incoming electron. Its wave function can be decomposed into partial waves $\mu \equiv (l, m)$. As explained in Paper I, there are four electron partial waves, $\mu = s$, p_z, and $p_\pm = p_x \pm i p_y$ considered in our model, which are coupled to the discrete states $|d\rangle$ through the energy-dependent amplitudes $V_{d\epsilon}^{\mu}$ organized into the following 3×4 matrix [Eq. (18) in Paper I]:

$$V_\epsilon = \begin{array}{c} \\ \Pi_+ \\ \Sigma \\ \Pi_- \end{array} \begin{array}{c} \begin{array}{cccc} s & p_z & p_+ & p_- \end{array} \\ \begin{pmatrix} v_{\Pi s} Q_- & v_{\Pi z} Q_- Q_u & v_{\Pi p} & w_{\Pi p} Q_-^2 \\ v_{\Sigma s} & v_{\Sigma z} Q_u & v_{\Sigma p} Q_+ & v_{\Sigma p} Q_- \\ v_{\Pi s} Q_+ & v_{\Pi z} Q_+ Q_u & w_{\Pi p} Q_+^2 & v_{\Pi p} \end{pmatrix} \end{array}, \tag{13}$$

with row index d and column index μ. In this matrix we explicitly show the dependence on the vibrational coordinates Q_i that are not totally symmetric. Symmetric combinations of coordinates are still hidden in the coefficients $v_{d\mu}$ and $w_{d\mu}$ (Sec. IV B of Paper I).

For example, the first column of the matrix V_ϵ describes the attachment of an s-wave electron to the molecule given by the right-hand side $|\Phi\rangle$ Eq. (11) of the Schrödinger equation. Its vibrational parts $|\phi_d\rangle$ have the same symmetry as the coordinates in the first column of the matrix V_ϵ, i.e., Π_u, Σ_g^+, and Π_u, in order for the product of $|\phi_d\rangle$ and electronic part $|d\rangle$ to have the same symmetry as the incoming electron s wave, i.e., Σ_g^+. Since the symmetry is respected by the model quantities H_0, U, and $F(E)$, the same discussion applies for the components of the solution $|\Psi\rangle$ (9). The resulting symmetries of $|\psi_d\rangle$, $|\phi_d\rangle$ are listed in the first block of Table I. These symmetries can be observed in Fig. 4. The wave functions in the top row of the figure have symmetries Σ_g^+, Π_u, and Δ_g as apparent from their shape since the probability close to the zero axis of the bending coordinate is being pushed to higher bending values for a larger angular-momentum projection.

Due to the vibronic coupling built in the Q dependence of the matrix V_ϵ, the symmetry of the outgoing electron can differ from the symmetry of the incoming electron. This change has to be compensated by the final vibrational state of CO_2, that is, the product of the vibrational and electronic parts of the final $e + CO_2$ wave function has to have the same symmetry as the incoming electron. In our model, the final states of the Σ_g^+, Σ_u^+, Π_g, Π_u, and Δ_g symmetries can be excited, see the second block of Table I.

V. CALCULATED SPECTRA

Finally, we present the results of our calculations. We start with the spectrum calculated directly using harmonic basis as final states and then we describe the results of the transformation of the final states into Fermi-coupled basis, which could be more directly compared with experiments.

A. Spectrum with harmonic final states

The differential cross section $d\sigma_{\nu_f \leftarrow \nu_i}/d\Omega(\epsilon_i)$ for the vibrational excitation of the CO_2 molecule from the initial state $|\nu_i\rangle$ to the final state $|\nu_f\rangle$ is calculated from the T-matrix elements Eq. (12) by summing over initial μ_i and final μ_f partial waves including the proper angular factors for each symmetry of the final state. The formulas are given in Appendix D of Paper I and they also include the averaging over the orientation of the molecule.

The final 2D spectrum intensity $S(\epsilon_i, \Delta\epsilon)$ is obtained by identifying the energy loss $\Delta\epsilon = \epsilon_i - \epsilon_f = E_{\nu_f} - E_{\nu_i}$ for each final state and adding a Gaussian profile $f(x)$ with the full width at half maximum of 18 meV to the electron-loss lines to simulate the finite experimental resolution

$$S(\epsilon_i, \Delta\epsilon) = \sum_{\nu_f} \frac{d\sigma_{\nu_f \leftarrow \nu_i}}{d\Omega}(\epsilon_i) f(\Delta\epsilon - \Delta\epsilon_{\nu_f}). \tag{14}$$

Note that we also convolve the spectra with the incident electron energy resolution function but it does not effect significantly the results since the cross sections are rather smooth in ϵ_i.

Figure 5 shows the 2D energy-loss spectrum for harmonic final vibrational states of CO_2 and a scattering angle of 135°, where the Fermi resonance effect is not included. The harmonic spectrum is dominated by energy-loss peaks at positions of Σ_g^+ and Π_u harmonic states that belong to polyads $(n, 2m^0, 0)$ and $[n, (2m+1)^1, 0]$, respectively. Their energy losses are given by $\Delta\epsilon = N\omega_g$ and $N\omega_g + \omega_b$, $N = n + m = 0, 1, \ldots$, respectively. In the case of asymmetric stretching mode, only $(0, 0^0, 1)$ and $(0, 0^0, 2)$ states are significantly populated, especially near the threshold. The higher Σ_g^+ and Π_u polyads derived from the $(0, 0^0, 2)$ state are also clearly seen in the spectrum, although the magnitude of the signal is about three orders of magnitude smaller. Higher values of ν_u are not populated significantly but are included in the presented data.

The harmonic spectrum of Fig. 5 reproduces qualitatively the general shape of the spectrum seen in the current and previous experiments [13,14]. At low energy losses the signal starts directly at the threshold. In the $^2\Pi_u$ resonance region (incident energies 3–4 eV), the signal extends to the complete energy loss. The hint of the boomerang oscillations [4,58], which creates the diagonal rays in the spectrum, is also visible

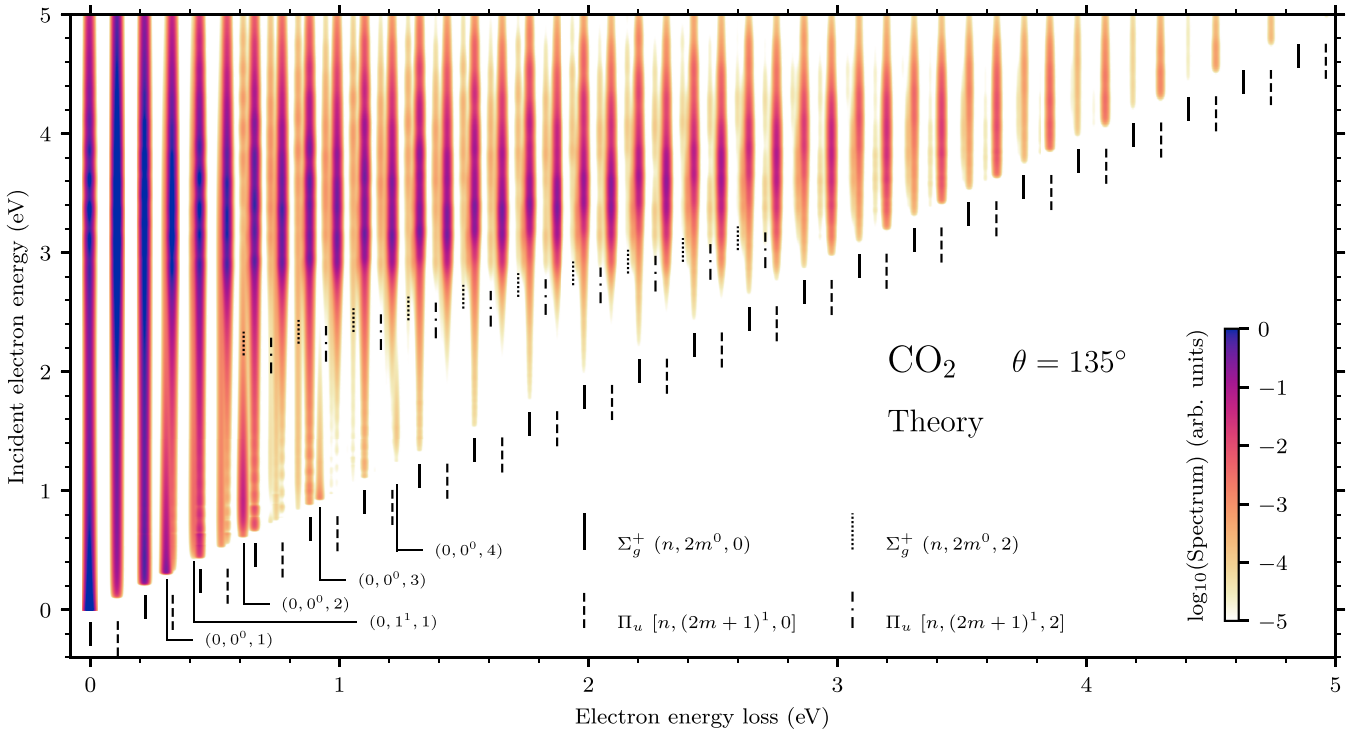

FIG. 5. Calculated 2D electron energy-loss spectrum of CO_2 for harmonic final vibrational states and for a scattering angle of 135°. Positions of some harmonic vibrational levels of CO_2 within our model are shown, see the legend ($n + m = 0, 1, \ldots$).

but their positions do not correspond to the experimental positions because of the substantial difference of our potentials along the symmetric stretching direction due to the harmonic approximation of the neutral molecule (Sec. V A of Paper I).

The most obvious difference between the experimental (Fig. 1) and theoretical (Fig. 5) spectra is the contrast between continuous character of the experimental spectrum and the discrete lines at specific energy losses dominating the theoretical spectrum. This is the effect of using the harmonic polyads (and their energies) as the final states in our calculations instead of the Fermi-coupled states. Let us also remind that the model vibrational frequencies are $\omega_b = 110$ meV, $\omega_g = 2\omega_b$, and $\omega_u = 308$ meV, which originate from the *ab initio* *R*-matrix data. The frequencies in the case of bending and symmetric stretching are about 30% larger than the experimental values and one symmetric stretching quantum is exactly degenerate with two quanta of bending (Sec. IV C in Paper I). The difference of the frequencies $\omega_s - 2\omega_b = 0.9$ meV does not explain the continuous character of the experimental spectrum since the highest polyads $N = 30$ fitting in the energy window still have energy spread comparable to the experimental resolution (Sec. III A). The Fermi coupling that mixes the states and splits their energies (Sec. III B) is responsible for the quasicontinuous character of the spectra. Note that in the energy range of interest the spectrum comprises of about 8000 states.

B. Spectrum with Fermi-coupled final states

To keep the calculations manageable, we restricted the model only to harmonic vibrations of the neutral molecule. The anharmonic terms are included in the dynamics of the temporary molecular anion through the dependence of the vibronic coupling matrices U and V_ϵ on the polynomials of the vibrational coordinates. For details, see Secs. IV and VI of Paper I. However, the harmonic states of the neutral CO_2 enter the nonlocal term $F(E - H_0)$ and the calculation of the T matrix Eq. (12) through the projection on the final harmonic vibrational state $|v_f\rangle$.

The first of these two approximations is important in order for the four-dimensional nonlocal dynamics to be manageable but the latter one is rather easily corrected by projecting the anionic wave function on the Fermi-coupled states $|\nu_{\rm FR}\rangle$, which are given by the expansion into the harmonic basis with the coefficients c_v [Eq. (6)]. In practice, such a projection to the Fermi-coupled state leads to the linear combinations of the harmonic T matrices:

$$T_{\nu_{\rm FR}\mu_f \leftarrow \nu_i\mu_i} = \sum_v c_v \, T_{v\mu_f \leftarrow \nu_i\mu_i}. \tag{15}$$

The differential cross sections $d\sigma_{\nu_{\rm FR}\leftarrow\nu_i}/d\Omega(\epsilon_i)$, given in Appendix D of Paper I for the harmonic final states, are then obtained by the same procedure in which the T matrices (15) replace the harmonic T matrices (12). Note that Rescigno *et al.* [35] used a similar procedure with mixing coefficients derived by Dennison [56] to compute the excitation of the members of the Σ_g^+ Fermi dyad from their population of harmonic states.

The 2D spectrum with the corrected final states is calculated in a straightforward manner using Eq. (14) with the cross sections $d\sigma_{\nu_{\rm FR}\leftarrow\nu_i}/d\Omega(\epsilon_i)$, the anharmonic energy losses $\Delta\epsilon_{\rm FR}$, and summed over all $\nu_{\rm FR}$. The remaining harmonic approximation inside $F(E - H_0)$ should have a smaller effect since the action of the nonlocal potential contains an average

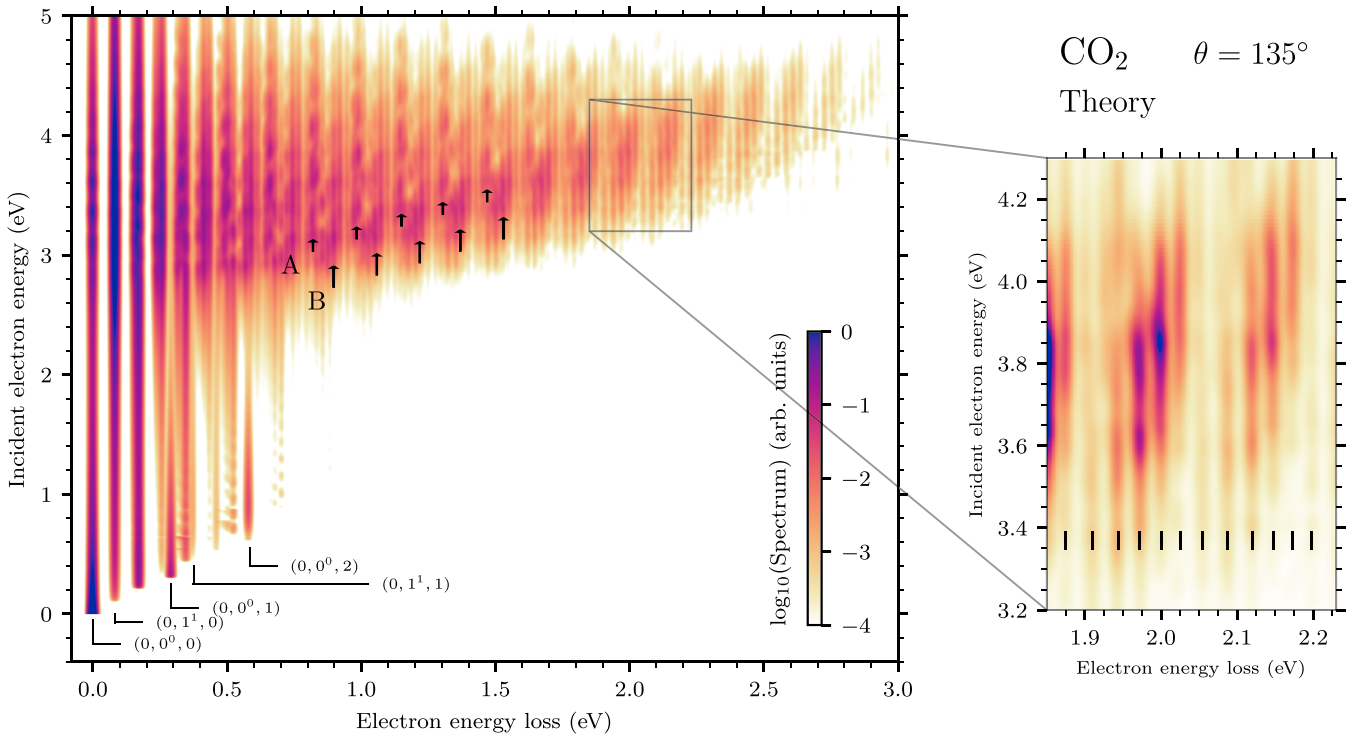

FIG. 6. Calculated 2D electron energy-loss spectrum of CO_2 for Fermi-coupled final vibrational states and a scattering angle of 135°. The magnified section of the signal (right—shown in linear scale from 0 to 1) focuses on a detail of the high energy loss features where the fine structure with spacing 25–33 meV is indicated. Structures *A* and *B* observed by Currell and Comer [12–14] are labeled in the main plot.

over many states in the harmonic approximation of H_0. The exception will be the threshold region, as discussed below.

Figure 6 shows the calculated 2D spectrum at 135° for the Fermi-coupled final vibrational states. As expected, the most obvious effect compared with the harmonic spectrum (Fig. 5) is the disappearance of the vertical bands associated with polyads in the deeply inelastic region. The spectrum also considerably shrinks in the energy-loss direction because of the 30% difference of the model and experimental vibrational frequencies. The vibrational Hamiltonian of Chedin [57] produces energies of the Fermi-coupled states that are in a very good agreement with spectroscopic data. The employed procedure corrects only the energy of the final electron. The dependence on the incoming electron is not effected. Therefore, the corrected 2D spectrum does not respect the threshold diagonal line, which is approximately 30% more steep and also broken. Also the Wigner cusps seen in some channels [33] do not have the correct position in our calculation, see the discussion below.

Despite these distortions, the spectrum in Fig. 6 qualitatively reproduces the measured spectrum in Fig. 1. We observe the boomerang rays although their exact positions are influenced by the distorted shape of the potentials. Both structures of type *A* and *B* discovered by Currell and Comer [13,14] are present and the fine structure at high energy losses has the correct shape, see below.

The qualitative agreement is even more apparent when 1D spectra are compared, see Fig. 7, where the spectra for incident energies 3.2, 3.5, 3.8, and 4.1 eV are plotted in the similar way as the experimental ones in Fig. 2. The spectra clearly follow the same pattern. At small energy losses we observe well-distinguishable peaks of the Σ_g^+ and Π_u symmetries, then a seemingly chaotic region (region II) occurs at intermediate energy losses, which is not as pronounced in the theory as in the experiment, and, finally, there are broad peaks modulated by the fine structure with spacing of 25–33 meV at the end of the spectra. The analysis that reveals the origin of these features is deferred to the next section. The very end of the spectra (dashed parts in Fig. 7) is an artifact caused by the above-mentioned inconsistency of the energies in the dynamics and the corrected energies of the Fermi-coupled levels. It only affects the near threshold region, i.e., high energy losses for incident energies in the region of the $^2\Pi_u$ resonance.

Although the fundamental asymmetric stretching mode $(0, 0^0, 1)$ is excited in our model (Figs. 5 and 6), it is excited by about one order of magnitude less in the region of the $^2\Pi_u$ resonance than experimental observations show [33] and is barely not visible in the 1D spectra. Our calculations only include the resonant (discrete-state) contribution to the vibrational excitation T matrix but we expect a considerable contribution of the background scattering to the elastic peak. It would also explain why the elastic cross section for a high scattering angle is less excited than the $(0, 1^1, 0)$ peak.

Before going to the detailed analysis of the spectra, we also look closer to the region of small initial electron energies ($\epsilon_i < 2.8$ eV), which is not covered by the current experimental data. The threshold region dominantly influenced by the $^2\Sigma_g^+$ virtual state of CO_2^- is visible in both calculated 2D spectra (Figs. 5 and 6). We would also like to remind a deficiency of our model that influences this region. The

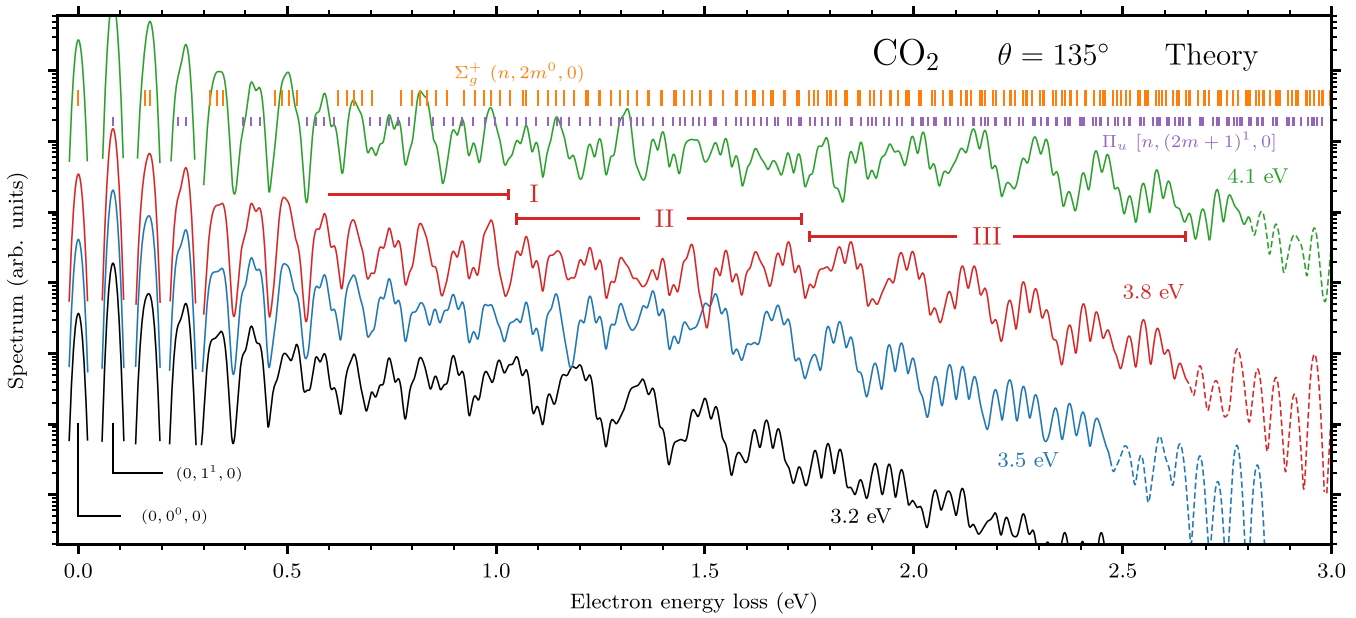

FIG. 7. Calculated 1D electron energy-loss spectra for Fermi-coupled final vibrational states and for a scattering angle of 135° and incident electron energies 3.2, 3.5, 3.8, and 4.1 eV. The spectra are shown in the logarithmic scale but lines for different incident energies are arbitrarily shifted with respect to each other. Calculated energies of states within Σ_g^+ $(n, 2m^0, 0)$ and Π_u $[n, (2m+1)^1, 0]$ Fermi polyads $(n + m = 0, 1, \ldots)$ are shown. Regions of order, chaos, and order observed by Allan [10] are labeled by I, II, and III for the 3.8 eV spectrum. The very end of the spectra near the threshold line (dashed parts) is an artifact of the anharmonic correction of final-state energies, see the text.

CO_2 molecule acquires a dipole moment upon bending or asymmetric stretching, which is not included in our model because the geometry dependence of the threshold exponent of the coupling amplitudes $V^{\mu}_{d\epsilon}$ would substantially increase the computational cost of the dynamics. As a result, threshold peaks are not as sharp and pronounced as in the experiments [32,33]. The cross sections will be discussed in Sec. VI D.

The calculations reproduce the selectivity of the low-lying Fermi-coupled states near the threshold and in the region of the $^2\Pi_u$ resonance observed by Allan [32,33], see Fig. 8. Allan reached an astonishing resolution of 7 meV, therefore, we used the same value in Eq. (14) to produce Fig. 8. To avoid the above-mentioned artifacts near the main diagonal in the spectrum, we chose slightly higher final energy (0.12 eV) in Fig. 8 in comparison with 0.05 eV of Allan [32].

The top members of the polyads are dominantly excited at the threshold because the vibrational wave function of these members reaches the closest to the region where the anionic and neutral potentials cross, see Vanroose *et al.* [37], who reproduced such a behavior for the Σ_g^+ polyads. The Π_u polyads follow the same mechanism. At small incident energies, our $(0, 1^1, 0)$ peak is suppressed in comparison to the experiment due to the missing dipole in our model.

VI. ANALYSIS OF THE RESULTS

In Secs. II and V, we have presented the obtained experimental and theoretical results. Here, we focus on a further analysis of the calculations to understand the underlying mechanisms. We start by decomposing the spectra based on vibrational state symmetries and electron partial waves. Then, we examine which states within the vibrational pseudocontinua are dominantly excited and we describe propensity rules in terms of wave functions. We use the obtained insight to interpret the experimental data and also discuss the angle dependence. We conclude this part by discussing the energy

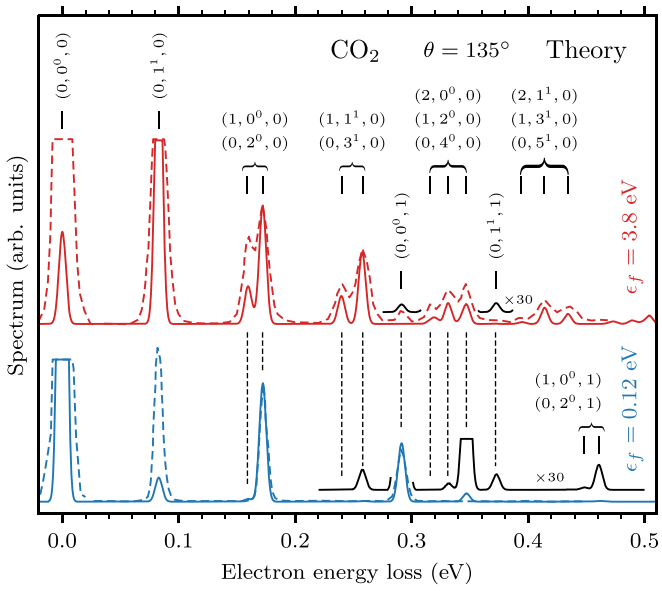

FIG. 8. Calculated 1D energy-loss spectra for fixed final electron energy of 0.12 eV (lower solid line) and 3.8 eV (upper solid line) and for a scattering angle of 135°. The calculations are compared with experimental data of Allan [32] (dashed lines) measured at final energies of 0.05 and 3.8 eV, see the text. The data are normalized to the upper peak of the Σ_g^+ dyad at 0.172 eV. Some peaks are cut off for clarity.

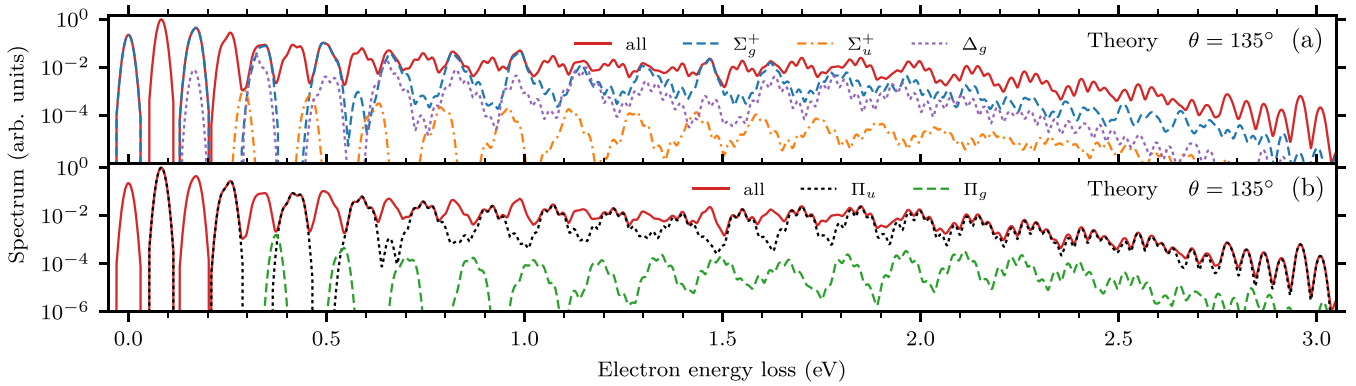

FIG. 9. Decomposition of the calculated 1D electron energy-loss spectrum for a scattering angle of 135° and incident electron energy of 3.8 eV to contributions of individual symmetries of final vibrational states. (a) Contributions of Σ_g^+, Σ_u^+, and Δ_g symmetries. (b) Contributions of Π_u and Π_g symmetries.

dependence of cross sections for low-lying final vibrational states.

A. Dominant vibrational state symmetries

We can decompose the 1D energy-loss spectrum based on final-state symmetries included in our model (Σ_g^+, Σ_u^+, Π_g, Π_u, and Δ_g), see Fig. 9. The spectrum is almost completely described by excitation of Σ_g^+ and Π_u vibrational states, from which the Fermi polyads $(n, 2m^0, 0)$ and $[n, (2m+1)^1, 0]$ dominate. States within Σ_g^+ $(n, 2m^0, 2)$ and Π_u $[n, (2m+1)^1, 2]$ polyads are included in the contributions shown in Fig. 9 but they are negligible as is apparent from the harmonic 2D spectrum in Fig. 5. States of the Δ_g symmetry are moderately excited throughout most of the spectrum but they are masked by similar energy dependence of the Σ_g^+ states. The Σ_u^+ and Π_g states, containing at least one excitation of the asymmetric stretching, do not contribute substantially.

The selection rules [41,42,59] predict strong excitation of Σ_g^+ and Δ_g vibrational states since they belong to the symmetrized square of the Π_u representation of the $^2\Pi_u$ resonance[2] and the excitation of the Π_u symmetry because the electron leaves as an s wave, see Sec. I. Overall, the results in Fig. 9 are in accordance with the selection rules. The mutual ratio of the Σ_g^+ and Δ_g is the result of the dynamics.

The decomposition of the spectrum to symmetries of the final states is straightforward since it is just a separation of different symmetries in the sum over all states in Eq. (14). The contributions of the individual electron partial waves are more easily identified in the spectrum integrated over all scattering angles, which we can calculate also from Eq. (14) by replacing the differential cross sections $d\sigma_{\nu_{\rm FR}\leftarrow\nu_i}/d\Omega(\epsilon_i)$ with the integrated ones:

$$\sigma_{\nu_{\rm FR}\leftarrow\nu_i}(\epsilon_i) = \frac{2\pi^3}{\epsilon_i} \sum_{\mu_i,\mu_f} |T_{\nu_{\rm FR}\mu_f\leftarrow\nu_i\mu_i}|^2. \tag{16}$$

[2]Characters of the symmetrized square of a representation are given by $[\chi^2](R) = [\chi(R)^2 + \chi(R^2)]/2$, where R denotes the symmetry operation [41].

Figure 10 shows the dominant contributions to the integral energy-loss spectrum in terms of incoming and outgoing partial waves. As shown in Table I, to excite the totally symmetric Σ_g^+ states, the electron symmetry does not change during the process and we have four contributions: $s \to s$, $p_z \to p_z$, $p_+ \to p_+$, and $p_- \to p_-$. The $p_z \to p_z$ process is negligible and $p_+ \to p_+$ and $p_- \to p_-$ give the same contribution. In the case of Π_u states, there has to be a change of the angular momentum, thus, they can be excited via $p_\pm \to s$ or $s \to p_\pm$ processes.

The attaching s wave contributes almost equally to the elastic peak and the $(0, 1^1, 0)$ peak as the $p_\pm$ waves. The $p_\pm$ attachment is expected to be dominant since $p_\pm$ are the principal partial waves of the $^2\Pi_u$ shape resonance. As we will see below, the Σ_g^+ virtual state does not significantly affect the dynamics at incident energies around 3.8 eV, therefore, the s wave also substantially populates the $^2\Pi_u$ resonance. The s wave cannot populate the resonance at the equilibrium linear geometry but due to the delocalized nature of the initial vibrational state $|\nu_i\rangle$, it attaches through the exponential tails to the $\Pi_\pm$ discrete states. Such a weaker attachment is compensated by the prefactor function $v_{\Pi s}$ [Eq. (13)], which is also responsible for the rapid broadening of the resonance width of the lower Renner-Teller component upon bending. For details see potentials in Fig. 4(b) and Sec. V B in Paper I.

In Fig. 10, we also observe a selectivity of the outgoing electron. Independently of the incoming partial wave, the outgoing s electron dominates over $p_\pm$ electrons at high energy losses, which is the consequence of Wigner threshold law [60]. The partial resonance widths $2\pi|V^\mu_{d\epsilon}|^2$ behave near the threshold as $\epsilon^{(2l+1)/2}$ with $l = 0, 1$ for s, p electrons. Thus, the electron preferentially detaches from the molecular anion as the s wave at small final energies.

B. Excitation of individual states and fine structure

We have seen that the Σ_g^+ $(n, 2m^0, 0)$ and Π_u $[n, (2m+1)^1, 0]$ Fermi polyads dominate the spectrum. Now, we pinpoint the states responsible for the observed structures emerging from the vibrational pseudocontinua.

We can analyze the contribution of individual final states to the theoretical spectrum in terms of the quantity $\langle v_g \rangle$,

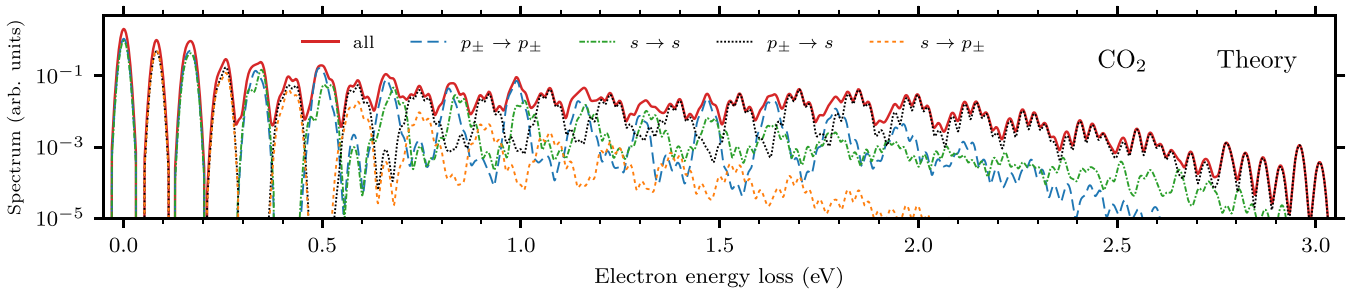

FIG. 10. Decomposition of the calculated integral 1D electron energy-loss spectrum for incident electron energy of 3.8 eV to contributions of individual incoming and outgoing partial waves. Processes $p_\pm \to p_\pm$ and $s \to s$ leads to excitation of Σ_g^+ vibrational states while Π_u states are excited when $p_\pm \to s$ and $s \to p_\pm$.

see Eq. (7). Figure 11 shows the calculated cross sections $d\sigma_{\nu_{\rm FR}\leftarrow\nu_i}/d\Omega(\epsilon_i)$ entering the sum in Eq. (14) for the spectrum with the Fermi-coupled states $|\nu_{\rm FR}\rangle$ grouped into the polyads (full symbols) in combination with the $\langle\nu_g\rangle$ values (open symbols). In the case of the Σ_g^+ $(n, 2m^0, 0)$ polyads [Fig. 11(a)], the states from the end of the polyads are dominantly excited for the lowest polyads but as the energy loss increases we observe a shift to excitation of the most linear states (largest $\langle\nu_g\rangle$). Typically, only two to three states from one polyad are excited enough to visibly affect the spectrum. The trend is similar but to some degree different for the Π_u symmetry [Fig. 11(b)]. The significance of peaks shifts from the end of the polyads to states at fixed positions (fifth and sixth states) somewhat in front of the maximum of $\langle\nu_g\rangle$.

The individual polyads within one symmetry dominate at different energy-loss ranges and the excitation of the several consecutive fairly linear states gives rise to the fine structure, whose energy spacing is not constant but varies around 25–33 meV. A detail of the fine structure is also shown in Fig. 4 in Letter.

To understand why only fairly linear states are significantly excited, we have to look at the wave functions. In Fig. 4, we have presented the scattered wave function $|\Psi\rangle$, which illustrates the dynamics even though we work in the time-independent picture. The initial vibrational state of CO_2^- is given by the wave function $|\Phi\rangle$ [Eq. (11)], that is, we have Gaussian packets modified by the coupling amplitude $V_{d\epsilon_i}^{\mu_i}$ on each potential-energy surface. Then, the wave packets move predominantly along the symmetric stretching coordinate since only in this direction there is a nonzero gradient at the equilibrium geometry. As the anion symmetrically stretches, the wave packets probe bent geometries too but the anion decays with a high probability by the electron autodetachment because of the large resonance width of the lower Renner-Teller component of the $^2\Pi_u$ resonance. This results in the significant suppression of the scattered wave functions at highly bent configurations in comparison to the vicinity of the symmetric stretching axis (Fig. 4). But note that the wave function still fills the energy-allowed region, see the contours of the lowest adiabatic potential in the top left panel of Fig. 4.

The dynamics is also confined in the asymmetric stretching because the potentials are repulsive in addition to the missing gradient at the equilibrium geometry. The excitation of vibrational states is controlled by the T-matrix element (12) and, thus, the states that have the probability density localized along positive symmetric stretches are dominantly populated, see the vibrational wave functions in Fig. 3. Moreover, the $^2\Sigma_g^+$ virtual state has a negligible effect on the spectra for incident energies above ∼3 eV since the magnitude of the Σ component $|\psi_\Sigma\rangle$ of the anionic wave function is substantially

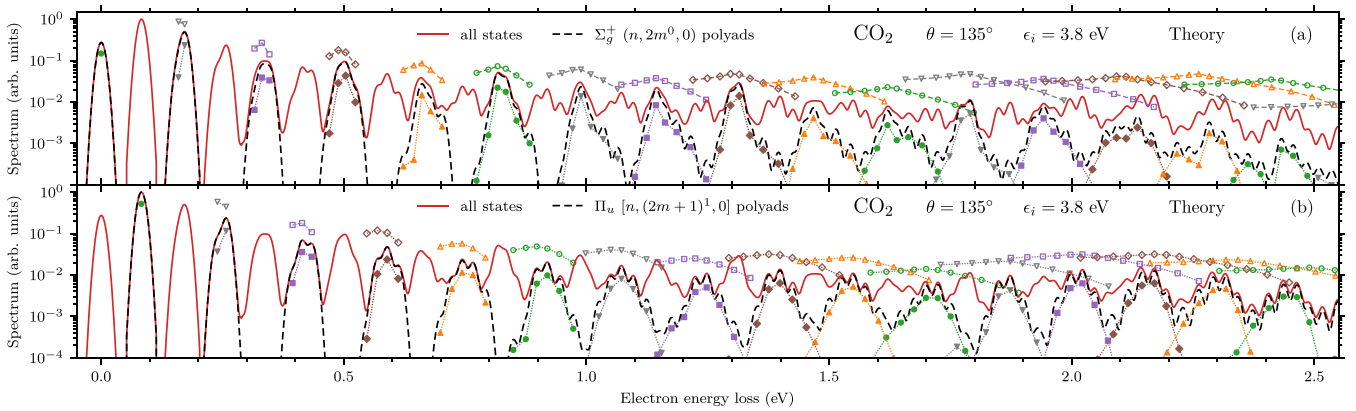

FIG. 11. Analysis of calculated 1D electron energy-loss spectrum for a scattering angle of 135° and incident electron energy of 3.8 eV. Full symbols represent the calculated cross sections (scaled down with respect to the spectrum for clarity) for exciting individual Fermi final vibrational states grouped into polyads. For each final state, the value of number of symmetric stretching quanta $\langle\nu_g\rangle$ (arbitrarily scaled) is shown by the open symbol above the spectra to indicate the character of the state, see the text. (a) Final states that belong to Σ_g^+ $(n, 2m^0, 0)$ Fermi polyads. (b) Π_u $[n, (2m+1)^1, 0]$ Fermi polyads $(n + m = 1, 2, \ldots)$.

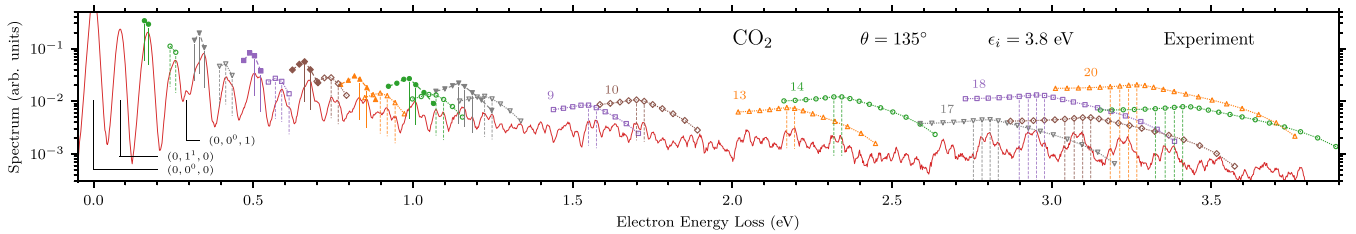

FIG. 12. Analysis of experimental 1D electron energy-loss spectrum for a scattering angle of 135° and incident electron energy of 3.8 eV. Symbols represent the theoretical energy and the value of number of symmetric stretching quanta $\langle v_g \rangle$ (arbitrarily scaled) for vibrational states grouped into Fermi polyads. Full symbols show Σ_g^+ $(n, 2m^0, 0)$ polyads with $n + m = 1, 2, \ldots, 7$. Open symbols show Π_u $[n, (2m + 1)^1, 0]$ polyads with $n + m = 1, 2, \ldots, 7, 9, 10, 13, 14, 17, \ldots, 21$. Note that there are $N + 1$ states for a polyad with $n + m = N =$ const.

smaller than the magnitude of the $\Pi_\pm$ components (Fig. 4). This was directly confirmed by calculations where the Σ discrete state was absent, see also Secs. VI D and VII B.

Now, we can confront these findings with the experiment, see Fig. 12 where the full and open symbols represent the $\langle v_g \rangle$ quantity for states within the Σ_g^+ and Π_u polyads, respectively. We observe the same trend of shifting the significance of the states within the polyads. It is not as clear for the Σ_g^+ symmetry because the shift towards the most linear states is somewhat slower and they soon disappear in the middle "chaotic" region, but the Π_u states distinctly follow the pattern. This time, the high energy-loss region (around 3 eV) is dominated by excitation of states at around the seventh and eighth positions within the Π_u polyads, see the last column in Fig. 3.

To summarize, the competition of the Σ_g^+ $(n, 2m^0, 0)$ and Π_u $[n, (2m + 1)^1, 0]$ Fermi polyads explains the shape of the energy-loss spectra. The peaks are well separated in region I since the polyads do not overlap (Figs. 2 and 7). The complex region II is given by the overlapping Σ_g^+ and Π_u contributions, which have similar magnitudes. As the energy loss increases the selectivity of the outgoing s-wave electrons starts to favor the Π_u states, which dominate in region III and are responsible for the broad peaks. The A and B structures of Currell and Comer [13,14] originate from the Σ_g^+ and Π_u contributions, respectively.

C. Angular dependence

We also investigated the angular dependence of the calculated energy-loss spectrum for incident electron energy of 3.8 eV, see Fig. 13(a). The deeply inelastic region (above 1.8 eV) is almost independent of the angle, which is consistent with our interpretation in terms of final Π_u states dominated by the $p_\pm \to s$ change of the electron partial waves, where the outgoing s wave leads to the isotropic character. To further experimentally verify this mechanism, we measured the spectrum for the scattering angles $\theta = 10°$ and 45°, see Fig. 13(b). First, we should explain an experimental artifact with respect to the data in Fig. 13(b). The analyzer sensitivity for the recording of slow electrons is very low for small scattering angles. This is manifested as an artificial cutoff of the spectrum at near complete energy losses (for $\theta = 10°$ the electrons with residual energies below 300 meV are not recorded, electrons slower than 100 meV are missing for 45°). The most probable reason for this cutoff is charging of the analyzer entrance slit

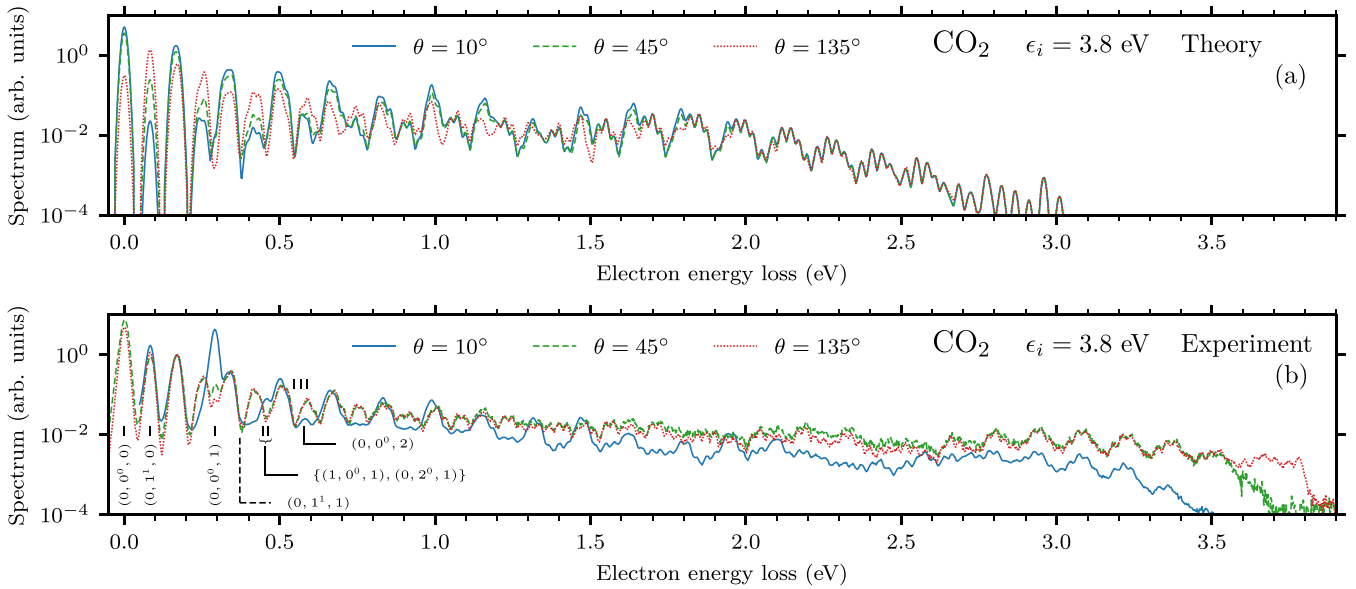

FIG. 13. Dependence of the electron energy-loss spectra at incident electron energy of 3.8 eV on the scattering angle θ for (a) the calculations and (b) the experiment.

by the primary electron beam. Also note that we normalized the experimental spectra to coincide at the peak of the Σ_g^+ Fermi dyad $\{(1, 0^0, 0), (0, 2^0, 0)\}$, which is assumed to be relatively weakly dependent on the angle. The theoretical spectra are calculated with the same mutual normalization.

Truly, the shape of the experimental broad peaks at high energy losses (∼3 eV) depends weakly on the scattering angle. For smaller energy losses, the Π_u peaks are suppressed at small angles because the $s \rightarrow p_\pm$ transition contributes while the Σ_g^+ peaks depend weakly on the angle, which is also consistent with previous measurements [10,17,18,27–31]. The analysis of the experimental spectrum for $\theta = 10^\circ$ in terms of the $\langle v_g \rangle$ quantity, see the previous section, confirms that the broader peaks at moderate energy losses are of the Σ_g^+ symmetry centered at the most linear states.

Overall, we cannot expect a good agreement between our calculations and the experiments for the angular dependence. First, the direct scattering due to the dipole acquired at distorted geometries, which is not included in our model, significantly affects the elastic peak $(0, 0^0, 0)$ and principal excitation $(0, 1^1, 0)$ and $(0, 0^0, 1)$ [17,18]. Second, our *R*-matrix calculations show that *d* and *f* waves strongly contribute to the $^2\Pi_u$ resonance but we limited the model to the lowest partial waves needed to excite all fundamental modes. Our *s*- and *p*-wave model includes higher partial waves in an averaged sense since we fit the scattering eigenphase sums and so we expect that the results will be more accurate for the integral cross sections rather then the differential ones. For details, see Sec. V C in Paper I.

In the experimental spectrum, the fundamental asymmetric stretching peak $(0, 0^0, 1)$ is strongly peaked in the forward direction and we also observe excitation of the Σ_u^+ Fermi dyad given by a mixture of harmonic states $(1, 0^0, 1)$ and $(0, 2^0, 1)$. Two quanta of asymmetric stretching $(0, 0^0, 2)$ seems to be visible at $\theta = 10^\circ$ but for higher angles the $(0, 0^0, 2)$ peak is hidden under the Π_u triad. On the other hand, we do not observe the $(0, 1^1, 1)$ peak of the Π_g symmetry for any angle at the incident energy of 3.8 eV.

D. Cross sections

Hitherto, we have analyzed the 2D spectrum from the point of view of the electron energy loss. In this section, we focus on the vibrational excitation cross sections; that is, 1D profiles along the incident electron energy axis for fixed energy loss corresponding to energies of individual final vibrational states of CO_2.

Figure 14 shows the differential cross sections for a scattering angle of 135° for excitation of various low-lying vibrational states of CO_2. As expected from the simplifications used in the model, we find only a qualitative agreement with experimental observations [33]. The resonance broad peak at 3–4 eV is modulated by the boomerang oscillations [4,58]. As was shown by Rescigno *et al.* [35] and we see it here in Sec. VII, these oscillations originate from the symmetric stretching and are dampen by the bending motion. In our calculations, the oscillations are more pronounced because they are sensitive to the shape of the potential, which substantially differs from the *ab initio* potential in our model due to the employed harmonic approximation for the neutral molecule.

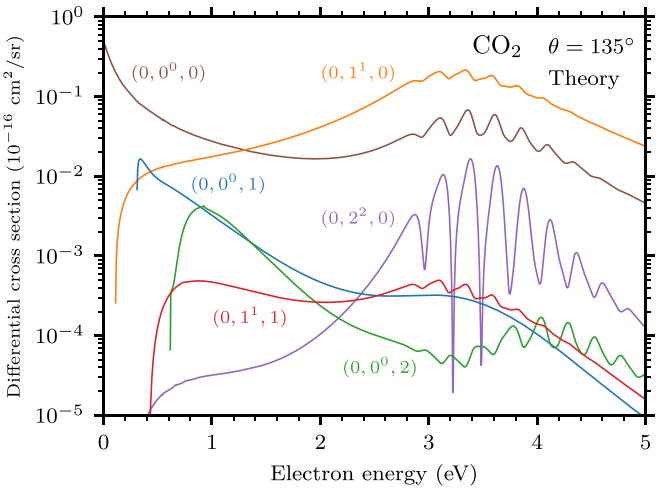

FIG. 14. Differential cross sections for vibrational excitation of CO_2 from initial state $(0, 0^0, 0)$ to final states: $(0, 0^0, 0)$, $(0, 1^1, 0)$, $(0, 0^0, 1)$, $(0, 2^2, 0)$, $(0, 1^1, 1)$, and $(0, 0^0, 2)$.

The elastic cross section is about order of magnitude less excited due to the missing direct background scattering in our calculations.

The excitation and selectivity of the members of the low-lying Σ_g^+ Fermi polyads (dyad, triad, ...) observed by Allan [32,33] and discussed here in Sec. V is already well reproduced by the theory thanks to the work of McCurdy *et al.* [34] and Vanroose *et al.* [37], who treated the threshold and resonance regions separately. We can provide a further insight, see Fig. 15, where the cross sections for the lower (I, $\Delta\epsilon = 0.159$ eV) and upper (II, $\Delta\epsilon = 0.172$ eV) members of the Σ_g^+ dyad are shown [Fig. 15(a)], in combination with

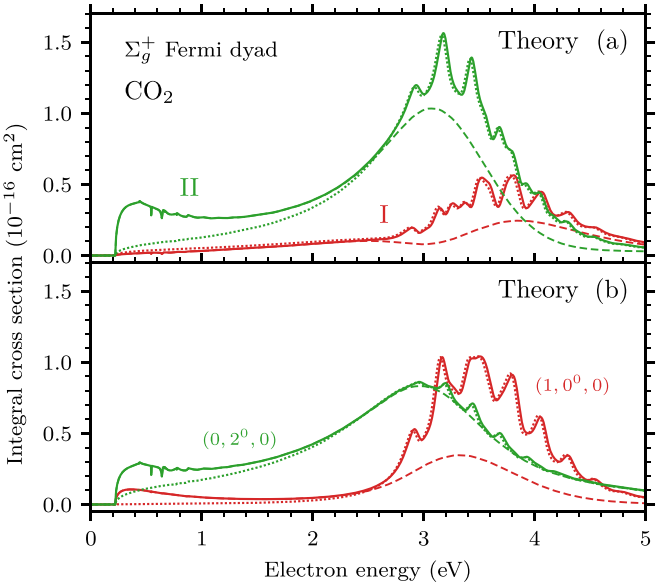

FIG. 15. Integral cross sections for vibrational excitation of CO_2 from initial state $(0, 0^0, 0)$ to members of the (a) Σ_g^+ Fermi dyad and (b) to harmonic states $(1, 0^0, 0)$ and $(0, 2^0, 0)$. Solid lines, full four-dimensional (4D) calculations; dashed lines, contribution of incoming *s* wave for 4D dynamics; dotted lines, calculations without the Σ_g^+ virtual state and without asymmetric stretching motion.

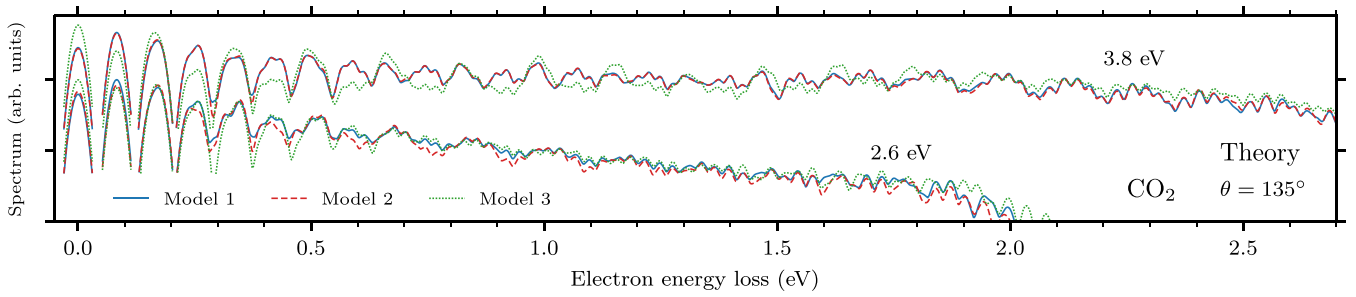

FIG. 16. Comparison of three constructed models in terms of calculated energy-loss spectra for a scattering angle of 135° and incident electron energy of 2.6 and 3.8 eV. The spectra are shown in the logarithmic scale but the two sets of data are arbitrarily shifted with respect to each other. Model 3 is not consistent with the *ab initio* data, see the text.

the harmonic states $(1, 0^0, 0)$ and $(0, 2^0, 0)$ that these members comprise of [Fig. 15(b)]. Except for the missing sharp threshold peak of the upper member, the general shape is well reproduced. The process $s \to s$ (dashed lines) overall dominates over $p_\pm \to p_\pm$ (the difference between full and dashed lines) and it contributes to the cross sections to both harmonic states, which results in the observed cancellation of the cross section for the lower member in the low to middle region [32] in comparison to Refs. [34,35].

Despite the interesting topology of the $1\,^2A_1$ and $2\,^2A_1$ potentials upon bending, we do not observe any related effects in the region of the $^2\Pi_u$ resonance, see dotted lines in Fig. 15, which were calculated without the Σ discrete state (all relevant parameters were set to zero). Without the Σ state, the lower Renner-Teller component is connected with the nonlinear minimum and the surfaces behave similarly to the model of McCurdy *et al.* [34] (Figs. 6 and 8 in Paper I). The region where the $1\,^2A_1$ potential crosses (or rather merges with) the neutral potential is important at very low incident energies (Fig. 15). For higher polyads $n + m \geqslant 2$, oscillatory structures appear in the cross sections [33,37]. In our calculations, we also observe such structures (visible in the 2D spectra in Figs. 5 and 6) but again their precise position is not reproduced due to the missing dipole and too large vibrational frequencies in the dynamics.

VII. SENSITIVITY OF THE RESULTS TO MODEL PARAMETERS

A. Sensitivity to values of parameters and fitting

The construction of a discrete-state-in-continuum model is inherently ambiguous because the discrete states are not uniquely defined. The ambiguity remains even though we have not constructed the model directly using the projection-operator approach [61], but we obtained the model parameters from *ab initio* eigenphase sums and potential energies. To validate the calculations, we constructed three models (Models 1, 2, 3) with the same parameter form but with different values. All presented results were calculated using Model 1, whose parameter values are given in Appendix C of Paper I. Model 2 behaves in the same way as Model 1. In these two models, the direct coupling λ of the Σ and $\Pi_\pm$ states have a small effect on the potential-energy surfaces. The primary effects upon bending (broadening of the lower Renner-Teller state, formation of the nonlinear minimum) are related to the indirect coupling through the s-wave continuum described by the parameter $v_{\Pi s}$.

Since we cannot distinguish between these two types of the coupling in the fitting procedure, we managed to construct Model 3 where the role of the parameters λ and $v_{\Pi s}$ is to a large degree interchanged; that is, the direct coupling λ has a significant effect on the potentials. Model 3 does not reproduce the *ab initio* eigenphase sums as well as Models 1 and 2 but still it reproduces them to a satisfactory level. However, we found that Model 3 is not consistent with the *ab initio* data because the resonance broadening is caused by the p wave instead of the s wave. For more details about the effect of model parameters on fixed-nuclei quantities, we refer the reader to Sec. V in Paper I, where the case of Model 1 is discussed.

Models 1 and 2 produce very similar spectra at the region of the $^2\Pi_u$ resonance, see Fig. 16. There is some quantitative difference for smaller incident energies but qualitatively both models behave the same. In the case of Model 3, the spectra for all final states do not look too different but contributions of individual final-state symmetries differ more substantially. Because of the inconsistency with the R-matrix data, we do not consider Model 3 to be physically relevant.

B. Dimensionality and electronic states

It is interesting to investigate the effect of freezing some of vibrational modes, which can be easily achieved in our model by reducing the basis in the corresponding dimension

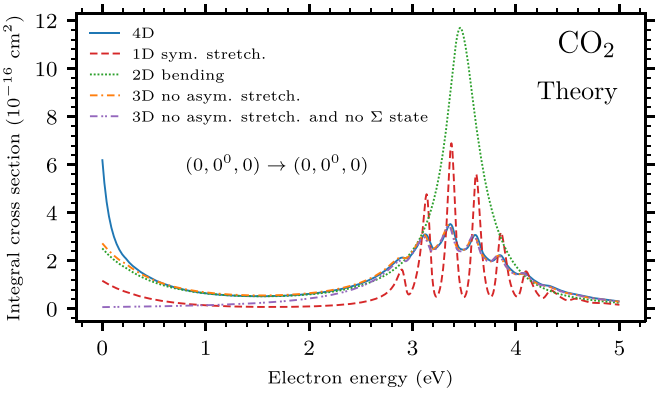

FIG. 17. Effect of the dimensionality of the dynamics on the integral elastic cross sections of CO_2. Both 3D calculations did not include the asymmetric stretching motion and in one case the Σ discrete state was excluded.

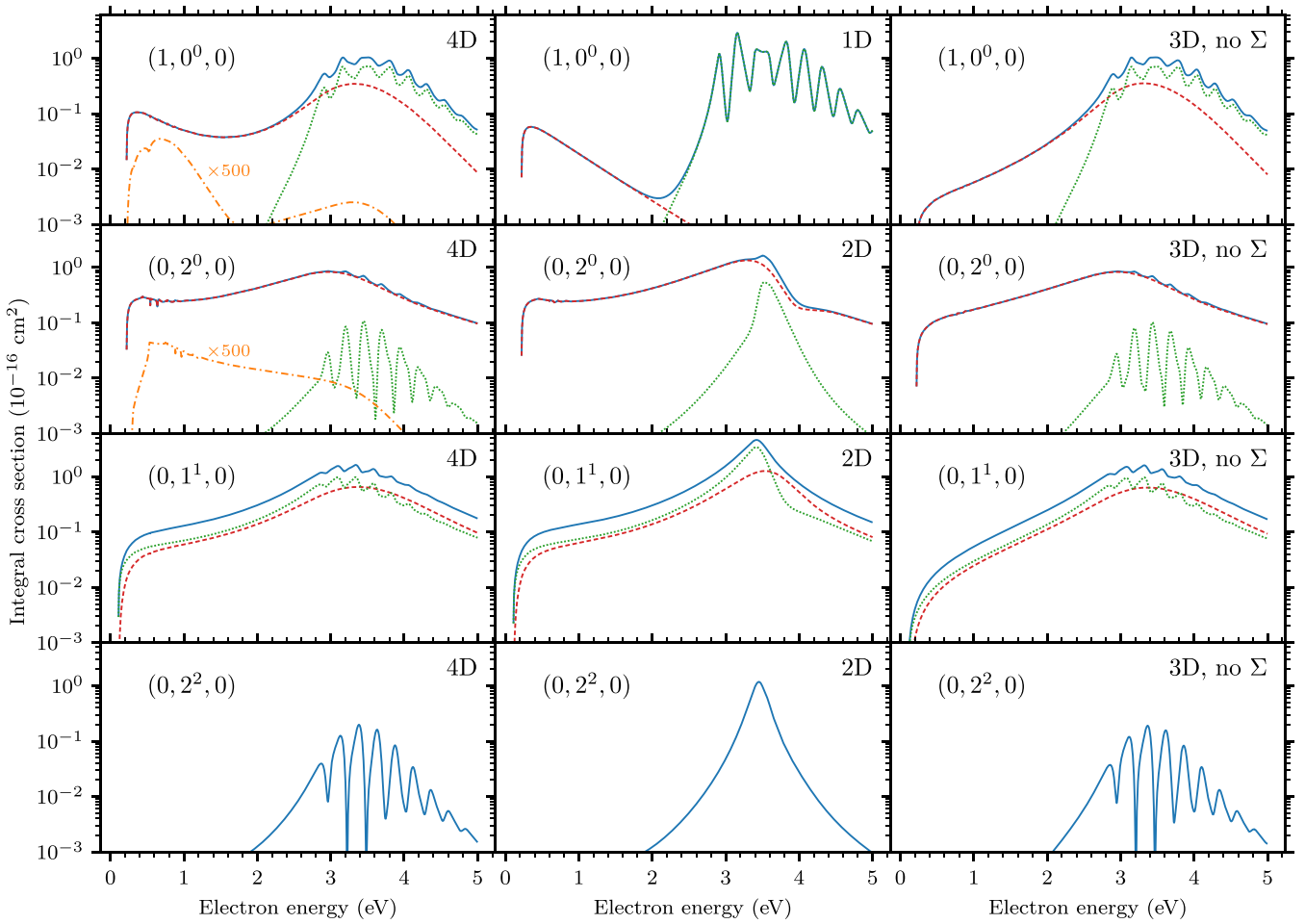

FIG. 18. Effect of the dimensionality of the dynamics on the integral cross sections for vibrational excitation of CO_2 from $(0, 0^0, 0)$ to four final harmonic states: $(1, 0^0, 0)$, $(0, 2^0, 0)$, $(0, 1^1, 0)$, and $(0, 2^2, 0)$ (in rows). First column, full 4D dynamics; second column, 1D dynamics in pure symmetric stretching for $(1, 0^0, 0)$ and 2D dynamics in pure bending for $(0, 2^0, 0)$, $(0, 1^1, 0)$, and $(0, 2^2, 0)$; third column, 3D dynamics without asymmetric stretching and without the Σ discrete state. Solid lines, contribution of all incoming electron partial waves; dashed lines, contribution of incoming s wave; dotted lines, contribution of incoming $p_\pm$ waves; dot-dashed lines, contribution of incoming p_z wave.

only to one state and setting appropriate parameters to zero. Such a reduction of the dimensionality is demonstrated for the elastic scattering in Fig. 17 and for the excitation of $(1, 0^0, 0)$, $(0, 2^0, 0)$, $(0, 1^1, 0)$, and $(0, 2^2, 0)$ harmonic states in Fig. 18, where also contributions of the individual incoming partial waves are shown when nonzero. The excitation of $(0, 2^2, 0)$ can only proceed via $p_\pm \to p_\mp$. We cannot perform 1D dynamics for pure asymmetric stretching motion, see below.

Upon pure symmetric stretching the threshold and resonance regions are well separated because the s wave cannot interact with the resonance. The boomerang oscillations originate in the symmetric stretching motion and are dampen by the broad resonance as the anion bends [34,35]. Moreover, the oscillations only occur if the electron comes in as p_+ or p_-. When the incoming electron is of the s-wave character, the formation of the $^2\Pi_u$ state forces the molecule to bend and the wave packet traveling along the symmetric stretch axis is a subject of the broader decay width. As a consequence, the oscillations of the anionic wave function along this axis are significantly suppressed (Fig. 4).

The whole dynamics is driven by the symmetric stretching vibrations because of the nonzero gradient. The pure bending motion leads to the cross sections with a structureless $^2\Pi_u$ peak, which is typically narrower and higher than the one in the case where the symmetric stretching is present. These results are similar to results of Laporta *et al.* [40] who performed 1D LCP calculations in each vibrational mode separately. In our model, we cannot perform 1D dynamics of the $^2\Pi_u$ doublet for pure asymmetric stretching motion because the p_z wave couples to the $\Pi_\pm$ discrete states only at combined asymmetrically stretched and bent geometries, see Eq. (13). Such 1D calculations are possible for an incoming d-wave electron, which is not included in our model.

Nevertheless, we do not expect 1D calculations of the vibrational motion in nontotally symmetric modes of polyatomic molecules to be appropriate in general. For such modes, potentials are even functions of the corresponding vibrational coordinates; that is, they possess no gradients at the equilibrium. They can play a key role as the bending does in the case of CO_2 but the dynamics in these modes alone is probably not sufficient. Moreover, if neutral and anionic potentials are close to being parallel and there is no symmetry breaking mechanism, the cross sections are strongly influenced by the fact that the neutral and anionic vibrational

states for different quanta are almost orthogonal to each other. We are convinced that this is the origin (not the boomerang effect) of structures in the cross sections upon asymmetric stretching presented in Ref. [40].

VIII. CONCLUSION

In conclusion, we summarize our join experimental and theoretical work on the vibrational excitation of CO_2 by slow electrons and we also discuss possible future improvements. The study comprises of our Letter [47] that outlines the primary results, the description of the theoretical model Ref. [48], and the detailed analysis of the results presented in this paper.

The theoretical work was motivated by three open challenges in the low-energy electron-molecule scattering. The first of them was the unexplained shape of the energy-loss spectra and the discovery of the fine structure with ∼30 meV spacing in our high-resolution 2D spectrum. The second challenge was the absence of the theoretical treatment of the interaction of the near threshold $^2\Sigma_g^+$ virtual state with the $^2\Pi_u$ resonance pointed out by Sommerfeld *et al.* [62] and hinted in experiments by Allan [32,33]. The last challenge was posed by the lack of development in the treatment of electron-molecule scattering by the nonlocal discrete-state-in-continuum model for polyatomic molecules including the vibronic coupling. The importance of the direct and indirect (through electron continuum) vibronic coupling was analyzed by Gallup [41]. However, only the direct vibronic coupling was previously included in the model study of 2D nonlocal dynamics by Estrada *et al.* [63] and in LCP calculations, e.g., by McCurdy *et al.* [34] for the $e + CO_2$ system (see also the introduction of Ref. [48]).

On the experimental side, we have presented the 2D energy-loss spectrum measured at the scattering angle of 135° with the energy resolution of 18 meV and to almost complete energy loss, in combination with additional 1D cuts for fixed incident energies at 10°, 45°, and 135°. The nuclear dynamics of the CO_2^- anion was modeled in the full vibrational dimensionality and in the presence of the $^2\Sigma_g^+$ virtual state and the $^2\Pi_u$ shape resonance coupled upon bending. We also included the vibronic coupling of these states to four electron partial waves s, p_z, $p_\pm$, which is the minimum set needed to explain the symmetries of all observed energy-loss peaks in the region up to 5 eV.

The inclusion of the vibronic coupling of the $^2\Pi_u$ resonance to the s-wave electron continuum is the most important aspect of the current model in comparison with previous calculations. It allows excitation of $^2\Pi_u$ vibrational states of CO_2, which have been found to dominate the highly inelastic region of the spectrum and their competition with $^2\Sigma_g^+$ states explains the shape of the spectrum. Only vibrational states that are localized in the vicinity of the symmetric stretching axis are significantly excited because the s-wave coupling causes an effective decay of the molecular anion at highly bent geometries. This selective mechanism gives rise to the observed fine structure with ∼30 meV spacing.

The interpretation of the fine structure by identification of the specific states from the quasicontinuum of energetically available final states is one of the primary successes of our model. Another achievement is the vibrationally complete description of the dynamics, which allows the prediction of all vibrational transitions experimentally observed. Moreover, the anionic wave functions (apart from giving aesthetic pictures) provide a further insight and interpretation for the results. The calculation also gives access to splitting of the dynamics based on irreducible representations of the molecular symmetry group and electron partial waves. Moreover, the possibilities of simplifying the dynamics were tested. This aspect may be important for treatment of larger molecules. In the case of CO_2, we have seen that the dynamics is driven by the symmetric stretching but the bending is important as well since it couples the states and partial waves. On the other side, the asymmetric stretching motion can be left out unless we are specifically looking into excitation of the energy-loss peaks associated with excitation of this motion. We have also discussed energy regions where the $^2\Sigma_g^+$ state or the $^2\Pi_u$ doublet can be omitted.

To achieve not only a qualitative but also quantitative agreement with the experimental data, several improvements of the model should be considered in the future. The most straightforward step is improving the quality of the potential-energy surfaces. However, it is difficult to reach a better correlation in the fixed-nuclei electron scattering to have a consistent set of data for the construction of the model. The harmonic approximation for the neutral vibrations should also be lifted to include the Fermi resonance directly into the dynamics. Furthermore, the inclusion of the dipole moment emerging upon bending and asymmetric stretching is necessary to precisely reproduce the threshold region and probably d and f waves are needed to improve the dependence on the scattering angle. The incorporation of the $O^- + CO$ dissociation channel that opens around 4 eV into the nuclear dynamics is the ultimate but computationally challenging goal since the dissociation proceeds via a conical intersection of the $^2\Pi_u$ resonance with another state of the $^2\Pi_g$ symmetry that is connected to the dissociation asymptote [64].

In the future, the present approach can also be applied to other molecules. The application should be rather straightforward, for example, for CS_2, which has the same symmetry as CO_2, or for linear molecules without inversion symmetry such as N_2O and OCS. The missing inversion symmetry would lead to a larger coupling of the two stretching vibrational modes. The treatment of the dynamics in the case of N_2O, for which a high-resolution measurement of Allan and Skalický [65] is available, would also be complicated by the presence of the dissociative attachment channel that opens below 1 eV. For molecules with the C_{2v} symmetry group (H_2O, NO_2), the construction of the model and calculation of the dynamics has to be modified but we do not expect large obstacles. A more challenging task is to apply the methods developed in this study for models of reduced dimensionality for larger molecules.

ACKNOWLEDGMENTS

We gratefully acknowledge the financial support provided by the Czech Science Foundation Projects No. 19-20524S (M.Č., K.H., J.D.), No. 20-11460S (J.F.), and No. 21-12598S (R.Č.) and by the Charles University Grant Agency, Project No. 552120 (J.D., M.Č.).

[1] C. Ramsauer, Über den wirkungsquerschnitt der kohlensäuremoleküle gegenüber langsamen elektronen, Ann. Phys. (Berlin, Ger.) **388**, 1129 (1927).

[2] M. Boness and J. Hasted, Resonances in electron scattering by molecules, Phys. Lett. **21**, 526 (1966).

[3] M. J. W. Boness and G. J. Schulz, Vibrational Excitation of CO_2 by Electron Impact, Phys. Rev. Lett. **21**, 1031 (1968).

[4] M. J. W. Boness and G. J. Schulz, Vibrational excitation in CO_2 via the 3.8-eV resonance, Phys. Rev. A **9**, 1969 (1974).

[5] I. Cadez, M. Tronc, and R. I. Hall, Oscillations in electron impact cross sections of CO_2 between 3 and 5 eV, J. Phys. B: At. Mol. Phys. **7**, L132 (1974).

[6] I. Cadez, F. Gresteau, M. Tronc, and R. I. Hall, Resonant electron impact excitation of CO_2 in the 4 eV region, J. Phys. B: At. Mol. Phys. **10**, 3821 (1977).

[7] A. Herzenberg, Oscillatory energy dependence of resonant electron-molecule scattering, J. Phys. B: At. Mol. Phys. **1**, 548 (1968).

[8] A. K. Kazansky and L. Y. Sergeeva, On the local theory of resonant inelastic collisions of slow electrons with carbon dioxide, J. Phys. B: At., Mol. Opt. Phys. **27**, 3217 (1994).

[9] A. Kazansky and L. Y. Sergeeva, A model study of vibrational excitation of carbon dioxide molecule by slow electrons: The role of wave packet sliding from the ridge, Z. Phys. D: At., Mol. Clusters **37**, 305 (1996).

[10] M. Allan, Study of triplet states and short-lived negative ions by means of electron impact spectroscopy, J. Electron Spectrosc. Relat. Phenom. **48**, 219 (1989).

[11] T. Reddish, F. Currell, and J. Comer, Studies of the 2 eV shape resonance in N_2 using a two-dimensional scanning technique, J. Phys. E: Sci. Instrum. **21**, 203 (1988).

[12] F. Currell and J. Comer, Polyatomic excitation effects observed in an electron impact study of the 4 eV shape resonance of carbon dioxide, J. Phys. B: At., Mol. Opt. Phys. **26**, 2463 (1993).

[13] F. Currell and J. Comer, Observation of Friction in the Nuclear Dynamics of CO_2^- Near the Equilibrium Geometry of the Negative Ion, Phys. Rev. Lett. **74**, 1319 (1995).

[14] F. Currell, Friction effects in excitation to high vibrational states of the electronic ground state of carbon dioxide via the 4 eV shape resonance, J. Phys. B: At., Mol. Opt. Phys. **29**, 3855 (1996).

[15] E. Fermi, Über den Ramaneffekt des Kohlendioxyds, Eur. Phys. J. A **71**, 250 (1931).

[16] G. Herzberg, *Molecular Spectra and Molecular Structure. Vol. 2: Infrared and Raman Spectra of Polyatomic Molecules* (Van Nostrand, New York, 1945).

[17] Y. Itikawa, Nonresonant vibrational excitation of CO_2 by electron collision, Phys. Rev. A **3**, 831 (1971).

[18] K. H. Kochem, W. Sohn, N. Hebel, K. Jung, and H. Ehrhardt, Elastic electron scattering and vibrational excitation of CO_2 in the threshold energy region, J. Phys. B: At. Mol. Phys. **18**, 4455 (1985).

[19] M. A. Morrison, N. F. Lane, and L. A. Collins, Low-energy electron-molecule scattering: Application of coupled-channel theory to e-CO_2 collisions, Phys. Rev. A **15**, 2186 (1977).

[20] M. A. Morrison, Interpretation of the near-threshold behavior of cross sections for e-CO_2 scattering, Phys. Rev. A **25**, 1445 (1982).

[21] B. L. Whitten and N. F. Lane, Near-threshold vibrational excitation in electron-CO_2 collisions: A simple model, Phys. Rev. A **26**, 3170 (1982).

[22] H. Estrada and W. Domcke, On the virtual-state effect in low-energy electron-CO_2 scattering, J. Phys. B: At. Mol. Phys. **18**, 4469 (1985).

[23] S. Mazevet, M. A. Morrison, L. A. Morgan, and R. K. Nesbet, Virtual-state effects on elastic scattering and vibrational excitation of CO_2 by electron impact, Phys. Rev. A **64**, 040701(R) (2001).

[24] L. A. Morgan, Virtual States and Resonances in Electron Scattering by CO_2, Phys. Rev. Lett. **80**, 1873 (1998).

[25] C.-H. Lee, C. Winstead, and V. McKoy, Collisions of low-energy electrons with CO_2, J. Chem. Phys. **111**, 5056 (1999).

[26] T. N. Rescigno, D. A. Byrum, W. A. Isaacs, and C. W. McCurdy, Theoretical studies of low-energy electron-CO_2 scattering: Total, elastic, and differential cross sections, Phys. Rev. A **60**, 2186 (1999).

[27] D. F. Register, H. Nishimura, and S. Trajmar, Elastic scattering and vibrational excitation of CO_2 by 4, 10, 20 and 50 eV electrons, J. Phys. B: At. Mol. Phys. **13**, 1651 (1980).

[28] T. Antoni, K. Jung, H. Ehrhardt, and E. S. Chang, Rotational branch analysis of the excitation of the fundamental vibrational modes of CO_2 by slow electron collisions, J. Phys. B: At. Mol. Phys. **19**, 1377 (1986).

[29] D. C. Cartwright and S. Trajmar, Resonant electron-impact excitation of vibrational modes in polyatomic molecules, J. Phys. B: At., Mol. Opt. Phys. **29**, 1549 (1996).

[30] M. Kitajima, S. Watanabe, H. Tanaka, M. Takekawa, M. Kimura, and Y. Itikawa, Strong mode dependence of the 3.8-eV resonance in CO_2 vibrational excitation by electron impact, Phys. Rev. A **61**, 060701(R) (2000).

[31] M. Kitajima, S. Watanabe, H. Tanaka, M. Takekawa, M. Kimura, and Y. Itikawa, Differential cross sections for vibrational excitation of CO_2 by 1.5-30 eV electrons, J. Phys. B: At., Mol. Opt. Phys. **34**, 1929 (2001).

[32] M. Allan, Selectivity in the Excitation of Fermi-Coupled Vibrations in CO_2 by Impact of Slow Electrons, Phys. Rev. Lett. **87**, 033201 (2001).

[33] M. Allan, Vibrational structures in electron CO_2 scattering below the $^2\Pi_u$ shape resonance, J. Phys. B: At., Mol. Opt. Phys. **35**, L387 (2002).

[34] C. W. McCurdy, W. A. Isaacs, H.-D. Meyer, and T. N. Rescigno, Resonant vibrational excitation of CO_2 by electron impact: Nuclear dynamics on the coupled components of the $^2\Pi_u$ resonance, Phys. Rev. A **67**, 042708 (2003).

[35] T. N. Rescigno, W. A. Isaacs, A. E. Orel, H.-D. Meyer, and C. W. McCurdy, Theoretical study of resonant vibrational excitation of CO_2 by electron impact, Phys. Rev. A **65**, 032716 (2002).

[36] C. W. McCurdy and J. L. Turner, Wave packet formulation of the boomerang model for resonant electron–molecule scattering, J. Chem. Phys. **78**, 6773 (1983).

[37] W. Vanroose, Z. Zhang, C. W. McCurdy, and T. N. Rescigno, Threshold Vibrational Excitation of CO_2 by Slow Electrons, Phys. Rev. Lett. **92**, 053201 (2004).

[38] J. P. Gauyacq and A. Herzenberg, Nuclear-excited Feshbach resonances in $e + HCl$ scattering, Phys. Rev. A **25**, 2959 (1982).

[39] W. Vanroose, C. W. McCurdy, and T. N. Rescigno, Scattering of slow electrons by polar molecules: Application of effective-range potential theory to HCl, Phys. Rev. A **68**, 052713 (2003).

[40] V. Laporta, J. Tennyson, and R. Celiberto, Calculated low-energy electron-impact vibrational excitation cross sections for CO_2 molecule, Plasma Sources Sci. Technol. **25**, 06LT02 (2016).

[41] G. A. Gallup, Symmetry selection rules for vibrational excitation by resonant electron impact and a unified treatment of vibronic coupling between resonances and to the continuum: A complete symmetry analysis of vibrational excitation in benzene, J. Chem. Phys. **99**, 827 (1993).

[42] S. F. Wong and G. J. Schulz, Vibrational Excitation in Benzene by Electron Impact Via Resonances: Selection Rules, Phys. Rev. Lett. **35**, 1429 (1975).

[43] R. Čurík and P. Čársky, Vibrationally inelastic electron scattering on polyatomic molecules by the discrete momentum representation (DMR) method, J. Phys. B: At., Mol. Opt. Phys. **36**, 2165 (2003).

[44] R. Čurík, P. Čársky, and M. Allan, Vibrational excitation of methane by slow electrons revisited: Theoretical and experimental study, J. Phys. B: At., Mol. Opt. Phys. **41**, 115203 (2008).

[45] R. Čurík, I. Paidarová, M. Allan, and P. Čársky, Joint experimental and theoretical study on vibrational excitation cross sections for electron collisions with diacetylene, J. Phys. Chem. A **118**, 9734 (2014).

[46] R. Čurík, P. Čársky, and M. Allan, Electron-impact vibrational excitation of cyclopropane, J. Chem. Phys. **142**, 144312 (2015).

[47] J. Dvořák, M. Ranković, K. Houfek, P. Nag, R. Čurík, J. Fedor, and M. Čížek, Vibronic Coupling through the Continuum in the $e + CO_2$ System, Phys. Rev. Lett. **129**, 013401 (2022).

[48] J. Dvořák, K. Houfek, and M. Čížek, Vibrational excitation in the $e + CO_2$ system: Nonlocal model of $\Sigma\Pi$ vibronic coupling through the continuum, Phys. Rev. A **105**, 062821 (2022).

[49] M. Allan, Measurement of differential cross sections for excitation of helium by electron impact within the first 4 eV above threshold, J. Phys. B: At., Mol. Opt. Phys. **25**, 1559 (1992).

[50] M. Allan, Measurement of the elastic and $\nu = 0 \rightarrow 1$ differential electron–N_2 cross sections over a wide angular range, J. Phys. B: At., Mol. Opt. Phys. **38**, 3655 (2005).

[51] K. Regeta and M. Allan, Autodetachment Dynamics of Acrylonitrile Anion Revealed by Two-Dimensional Electron Impact Spectra, Phys. Rev. Lett. **110**, 203201 (2013).

[52] C. S. Anstöter, G. Mensa-Bonsu, P. Nag, M. Ranković, T. P. R. Kumar, A. N. Boichenko, A. V. Bochenkova, J. Fedor, and J. R. R. Verlet, Mode-Specific Vibrational Autodetachment Following Excitation of Electronic Resonances by Electrons and Photons, Phys. Rev. Lett. **124**, 203401 (2020).

[53] M. Allan, M. Lacko, P. Papp, Š.. Matejčík, M. Zlatar, I. I. Fabrikant, J. Kočišek, and J. Fedor, Dissociative electron attachment and electronic excitation in $Fe(CO)_5$, Phys. Chem. Chem. Phys. **20**, 11692 (2018).

[54] M. Ranković, P. Nag, M. Zawadzki, L. Ballauf, J. Žabka, M. Polášek, J. Kočišek, and J. Fedor, Electron collisions with cyanoacetylene HC_3N: Vibrational excitation and dissociative electron attachment, Phys. Rev. A **98**, 052708 (2018).

[55] Y. Itikawa, Electron-impact vibrational excitation of polyatomic molecules, Int. Rev. Phys. Chem. **16**, 155 (1997).

[56] D. M. Dennison, The infra-red spectra of polyatomic molecules. Part II, Rev. Mod. Phys. **12**, 175 (1940).

[57] A. Chedin, The carbon dioxide molecule: Potential, spectroscopic, and molecular constants from its infrared spectrum, J. Mol. Spectrosc. **76**, 430 (1979).

[58] K. Houfek, M. Čížek, and J. Horáček, On irregular oscillatory structures in resonant vibrational excitation cross-sections in diatomic molecules, Chem. Phys. **347**, 250 (2008).

[59] G. A. Gallup, Selection rules for vibrational energy loss by resonant electron impact in polyatomic molecules, Phys. Rev. A **34**, 2746 (1986).

[60] E. P. Wigner, On the behavior of cross sections near thresholds, Phys. Rev. **73**, 1002 (1948).

[61] W. Domcke, Theory of resonance and threshold effects in electron-molecule collisions: The projection-operator approach, Phys. Rep. **208**, 97 (1991).

[62] T. Sommerfeld, H.-D. Meyer, and L. S. Cederbaum, Potential energy surface of the CO_2^- anion, Phys. Chem. Chem. Phys. **6**, 42 (2004).

[63] H. Estrada, L. S. Cederbaum, and W. Domcke, Vibronic coupling of short-lived electronic states, J. Chem. Phys. **84**, 152 (1986).

[64] A. Moradmand, D. S. Slaughter, D. J. Haxton, T. N. Rescigno, C. W. McCurdy, T. Weber, S. Matsika, A. L. Landers, A. Belkacem, and M. Fogle, Dissociative electron attachment to carbon dioxide via the $^2\Pi_u$ shape resonance, Phys. Rev. A **88**, 032703 (2013).

[65] M. Allan and T. Skalický, Structures in elastic, vibrational, and dissociative electron attachment cross sections in N_2O near threshold, J. Phys. B: At., Mol. Opt. Phys. **36**, 3397 (2003).